The Influences of Land Use and Land Cover on Climate: An Analysis of the Washington-Baltimore Area That Couples Remote Sensing with Numerical Simulation

---

GEOLOGICAL SURVEY PROFESSIONAL PAPER 1099-A

U.S. DEPARTMENT OF THE INTERIOR

March 3, 1849

The Influences of Land Use and Land Cover on Climate: An Analysis of the Washington-Baltimore Area That Couples Remote Sensing with Numerical Simulation

By ROBERT W. PEASE, CAROL B. JENNER, *and* JOHN E. LEWIS, JR.

THE INFLUENCES OF LAND USE AND LAND COVER IN CLIMATE ANALYSIS

GEOLOGICAL SURVEY PROFESSIONAL PAPER 1099-A

An example of environmental analysis using
land use and land cover information

U.S. DEPARTMENT OF THE INTERIOR
March 3, 1849

UNITED STATES GOVERNMENT PRINTING OFFICE, WASHINGTON : 1980

UNITED STATES DEPARTMENT OF THE INTERIOR

CECIL D. ANDRUS, *Secretary*

GEOLOGICAL SURVEY

H. William Menard, *Director*

Library of Congress Cataloging in Publication Data

Pease, Robert W
The influences of land use and land cover on climate.

(Geological Survey professional paper ; 1099–A
Bibliography: p.
Supt. of Docs. no.: I 19.16:1099–A
1. Washington, D. C., region—Climate.
2. Baltimore region, Md.—Climate. 3. Land use— Washington, D. C., region. 4. Land use—Maryland—Baltimore region. I. Jenner, Carol B., joint author. II. Lewis, John E., 1937- joint author. III. Title. IV. Series: United States Geological Survey. Professional paper ; 1099–A.

QC984.D6P4 551.6'9'752 79–607068

For sale by the Superintendent of Documents, U.S. Government Printing Office
Washington, D.C. 20402

FOREWORD

The publication of the 1099-series of USGS Professional Papers represents the foundation of a new research area in climatology. This new field of investigation, termed "Land Use Climatology," promises to extend our understanding of earth-atmosphere interactions, especially as influenced by the surface energy budget. The papers in this series are an outgrowth of the Geological Survey's Central Atlantic Regional Ecological Test Site (CARETS) project, undertaken in coordination with, and with funding support from, the National Aeronautics and Space Administration.

The thrust behind the climate research in the CARETS project was threefold: (1) to define the relations between land use and land cover and several important climatic factors—relations that must be understood in order to evaluate accurately the climate effects of land use and land cover changes; (2) to demonstrate that the surface distributions of energy balance phenomena, as influenced by land use and land cover, could be mapped and analyzed from remotely sensed data; and (3) to demonstrate and verify the validity of numerical simulation modeling as a method for analyzing how various land use and climatic parameters are related.

This first paper, 1099-A, by Robert W. Pease, Carol B. Jenner, and John E. Lewis, Jr., encompasses all three objectives. It examines the nature and causes of relations between land use and land cover patterns and energy exchange phenomena using both remotely sensed data and simulation modeling. The second, 1099-B, by Wallace E. Reed and John E. Lewis, Jr., looks more closely at the first objective and describes how land use and land cover data were successfully used, in combination with air quality modeling, to estimate sulfur dioxide (SO_2) and particulate emissions, diffusion, and impact patterns. The third, 1099-C, by Francis W. Nicholas and John E. Lewis, Jr., concentrates on the relationship between land use and land cover and aerodynamic roughness, an essential input to climate simulation modeling. This study carefully describes the influence of various land use types on the turbulent transfer of energy to the atmosphere. The fourth study, 1099-D, by Carol B. Jenner and Robert W. Pease, compares two techniques for analyzing relationships between land use and surface radiation as measured by remotely sensed data. One is based on computer analysis by grid cells, the other is based on manual interpretation by polygons. Finally, the fifth, 1099-E, by Gordon M. Greene, examines the influences of several urban surface parameters, as determined by land use, on the urban thermal regime. This analysis is based on a test of the sensitivity of model-predicted surface temperatures to simulated changes in the urban surface parameters.

Although these studies are contributions to basic research, they also offer great potential in applications-oriented research. The techniques developed and tested in this professional paper series should prove to be an asset in the National Climate Program's analysis of relations between climate variability and land and water resources.

James R. Anderson

JAMES R. ANDERSON
Chief Geographer

CONTENTS

ILLUSTRATIONS

TABLES

SYMBOLS USED IN THIS TEXT

Symbol	Definition
a	Albedo.
a_1	Empirical constant of 0.55.
b	Empirical constant of 0.056.
c	Mass absorption coefficient.
c_1	First radiation constant in the Planck equation.
c_2	Second radiation constant in the Planck equation.
d	Dust and haze particle concentration, in particles per cubic centimeter.
d_1	Bulk diffusivity.
d_2	Thermal diffusivity.
e	Natural log base.
$f_{i,j,k}$	Frequency of land use type k within the cell i, j.
g	Acceleration of gravity, in centimeters per second squared.
h	Hour angle.
h_o	Obstacle height.
i	Slope of surface, in degrees above the horizon.
k	Von Kármán constant.
m	Optical air mass.
$\overline{m}$	Mean mixing ratio of atmosphere layer, in grams of water per kilogram of dry air.
n	Number of sample points in the grid cell.
p	Atmospheric pressure, in millibars.
p_2-p_1	Pressure depth of atmosphere layer, in millibars.
q	Diffuse incoming solar radiation.
q_{uprt}	Diffuse radiation received by a shadowed wall.
q_w	Specific humidity.
q'	Diffuse solar radiation downscattered as part of beam attenuation.
r	Flux of momentum near surface.
r_i	Instantaneous Earth-Sun distance.
r'	Earth-Sun distance when $r=1$.
$\overline{r}$	Mean Earth-Sun distance.
t	Time, in seconds.
u	Windspeed.
u^*	Friction velocity.
w	Water vapor, in precipitable centimeters (grams per square centimeter).
w_m	Precipitable water in the atmospheric column, in millimeters.
z	Height above surface.
z_d	Atmospheric damping depth.
z_s	Depth in the soil.
z_G	Soil damping depth.
z_0	Roughness length.
z_1	Soil depth 1.
z_2	Soil depth 2.
z_3	Soil depth 3.
A_0	A constant equal to 1.3114 ex-4.
A_1	A constant equal to 4.7650 ex-6.
B	Backscattered diffuse solar radiation.
C	Pulse code modulation (PCM) count.
C_P	Specific heat of air at constant pressure.
C_s	Soil volumetric heat capacity.
D	Spacing of obstacles.
$\overline{DP}$ °C	Mean dew point of air layer, in degrees Celsius.
$E_{bb}(\overline{T}°K)$	Blackbody equivalent of air column radiance for mean column temperature $\overline{T}$ in degrees Kelvin.
$E\uparrow$	Energy emitted by the surface.
$E\downarrow$	Energy absorbed by the surface.
F	View factor (Outcalt, 1971).
F'	View factor (Riefsnyder and Lull, 1965).
G	Flux of heat entering the soil.
G_0	Downward longwave radiation, in watts per square meter.
H	Kinetic or sensible heat flux into the atmosphere.
$\overline{H}\theta$	Mean height of objects above the surface.
I	Time increment.
I_0	Radiant signal emitted by the Earth's surface.
I_z	Radiant energy received aloft.
K	Thermal diffusivity value.
K_h	Turbulent diffusivity for heat.

Symbol	Definition
K_m	Eddy diffusivity for momentum.
K_w	Turbulent diffusivity for water vapor.
L	Latent heat of vaporization.
LE	Latent energy used in evapotranspiration.
P_v	Vapor pressure, in millibars.
Q	Direct solar radiation received at the surface, in watts per square meter.
$Q+q$	Incoming solar radiation, in watts per square meter.
Q_s	Solar radiation received at any moment upon an imaginary plane parallel with the Earth's surface and at the outer edge of the atmosphere, per unit area.
Q_{so}	Solar constant, in watts per square meter.
Q_{uprt}	Beam radiation received by an illuminated wall.
R	Radiance, in watts per square centimeter per steradian per micrometer.
R_{lw}	Longwave component of net radiation.
$R_{lw}\uparrow$	Longwave radiation emitted by the Earth's surface.
$R_{lw}\downarrow$	Longwave radiation emitted by the atmosphere.
R_n	Radiation balance at the terrestrial surface (net radiation).
R_{sw}	Shortwave component of net radiation.
$R_{sw}\uparrow$	Solar energy reflected by the Earth's surface.
$R_{sw}\downarrow$	Solar radiation incident upon the Earth's surface.
R_{uprt}	Total solar radiation received by a vertical wall.
R_z	Radiance received aloft.
R_{zH}	Radiance received aloft from a high-radiance calibration target.
R_{zL}	Radiance received aloft from a low-radiance calibration target.
R_0	Radiance emitted at the Earth's surface.
R_{zH}	Radiance emitted by a high-radiance calibration target.
R_{0L}	Radiance emitted by a low-radiance calibration target.
$R\uparrow$	Upward radiance of air layer, or upwelling radiation.
$R_1\uparrow$	Upward radiance of air layer 1.
$R_2\uparrow$	Upward radiance of air layer 2.
$R_3\uparrow$	Upward radiance of air layer 3.
$R_4\uparrow$	Upward radiance of air layer 4.
$R_5\uparrow$	Upward radiance of air layer 5.
$R_6\uparrow$	Upward radiance of air layer 6.
$R\uparrow a$	Upward radiance of air column.
$R\downarrow$	Downwelling radiation.
Ri	Bulk Richardson number.
S_1	Silhouette area of the average building.
S_2	Specific area, or the average lot area of each building.
SF	Shadow fraction.
T	Transmissivity of air.
T_2	Transmissivity of air layer 2.
T_3	Transmissivity of air layer 3.
T_4	Transmissivity of air layer 4.
T_5	Transmissivity of air layer 5.

Symbol	Definition
T_6	Transmissivity of air layer 6.
T_d	Temperature at the atmospheric damping depth.
$T_{i,j}$	Average surface temperature in a single square-kilometer grid cell.
T_k	Simulated temperature associated with land use and land cover type *k*.
T_s	Soil temperature.
$\overline{T}_{sky}$	Mean temperature of atmospheric downradiation, in degrees Kelvin.
T_t	Transmissivity of turbid air.
T_{tir}	Thermal infrared transmissivity of air.
T_{vis}	Visual transmissivity of turbid air.
T_{wv}	Transmissivity of air layer containing water vapor.
$T_{wv,t}$	Transmissivity of air layer containing water vapor, aerosols, and gaseous pollutants.
T_z	Temperature at screen height, in degrees Kelvin.
T_D	Dewpoint, in degrees Celsius.
$T°\mathrm{C}$	Temperature, in degrees Celsius.
$T_1°\mathrm{C}$	Soil temperature at depth 1, in degrees Celsius.
$T_2°\mathrm{C}$	Soil temperature at depth 2, in degrees Celsius.
$T_3°\mathrm{C}$	Soil temperature at depth 3, in degrees Celsius.
$\overline{T}°\mathrm{C}$	Mean temperature of air layer, in degrees Celsius.
T_0	Temperature of the Earth's surface, in degrees Kelvin.
$T°\mathrm{K}$	Temperature, in degrees Kelvin.
$\overline{T}°\mathrm{K}$	Mean temperature of air column, in degrees Kelvin.
V_M	Meteorological visibility.
$W\lambda$	Radiant energy, in watts per square centimeter per micrometer (Planck equation).
WF	Wet fraction.
Z	Solar zenith angle.
Z'	Solar zenith angle with respect to a sloping surface.
a	Solar azimuth angle, in degrees with respect to due south.
a'	Aspect of surface slope, in degrees with respect to due south.
δ	Solar declination.
ε	Emissivity.
γ	Extinction coefficient.
γ_{tir}	Thermal infrared extinction coefficient.
γ_{vis}	Visual extinction coefficient.
κ	Thermal diffusivity of soil.
λ	Wavelength interval in the sensing window.
ρ	Air density.
σ	Stefan-Boltzmann constant.
σ_{sw}	Shortwave scattering coefficient.
ϕ	Latitude.
Γ	Adiabatic lapse rate.
Θ	Potential temperature.
corr.	Slope correction factor.

THE INFLUENCES OF LAND USE AND LAND COVER IN CLIMATE ANALYSIS

THE INFLUENCES OF LAND USE AND LAND COVER ON CLIMATE: AN ANALYSIS OF THE WASHINGTON-BALTIMORE AREA THAT COUPLES REMOTE SENSING WITH NUMERICAL SIMULATION[1]

By ROBERT W. PEASE,[2] CAROL B. JENNER,[3] and JOHN E. LEWIS, JR.[4]

ABSTRACT

The Sun drives the atmospheric heat engine by warming the terrestrial surface which in turn warms the atmosphere above. Climate, therefore, is significantly controlled by complex interaction of energy flows near and at the terrestrial surface. When man alters this delicate energy balance by his use of the land, he may alter his climatic environment as well. Land use climatology has emerged as a discipline in which these energy interactions are studied; first, by viewing the spatial distributions of their surface manifestations, and second, by analyzing the energy exchange processes involved. Two new tools for accomplishing this study are presented: one that can interpret surface energy exchange processes from space, and another that can simulate the complex of energy transfers by a numerical simulation model. Use of a satellite-borne multispectral scanner as an imaging radiometer was made feasible by devising a gray-window model that corrects measurements made in space for the effects of the atmosphere in the optical path. The simulation model is a combination of mathematical models of energy transfer processes at or near the surface. Integration of these two analytical approaches was applied to the Washington-Baltimore area to coincide with the August 5, 1973, Skylab 3 overpass which provided data for constructing maps of the energy characteristics of the Earth's surface. The use of the two techniques provides insights into the relationship of climate to land use and land cover and in predicting alterations of climate that may result from alterations of the land surface.

INTRODUCTION

The impact of man's use of the land on both his local and worldwide climatic environment has become a significant concern. In its simplest terms, climate involves the characteristics and ongoing phenomena of the lower atmosphere that are controlled by the terrestrial surface over which the atmosphere lies or from which it has moved. The ultimate controls of the surface are its absorption of shortwave solar and downward longwave atmospheric radiation; the manipulation of the absorbed energy by the surface and the substrate; and the energy transfer back across the Earth-air interface, mostly to the overlying air but partly to outer space. The terrestrial surface and substrate thus act as intermediate agents in the climatic process, and the nature of the surface-air interactions must be understood because these agents are the driving forces that control the climatic environment.

The nature of the energy flow into and out of the surface and its substrate is complex and depends upon such factors as the amount of solar and atmospheric radiation reaching the surface, the portion of this energy that the surface will absorb, the heat capacity and diffusivity of the substrate, and the characteristics of the surface that control the movement of energy back into the atmosphere by radiant emission or turbulent transfer. As man alters the terrestrial surface, he changes this complex array of processes and alters his climatic environment, sometimes beneficially, but often in ways detrimental to his existence.

PURPOSE AND SCOPE

It is the purpose of this study to develop and examine ways to understand better the terrestrial surface and its interaction with the air above it. Techniques were developed for rapid measurement by satellite-borne electro-optical scanners of phenomena related to energy exchange across the surface-to-air interface. Computer techniques also were developed to replicate the same phenomena by means

---

[1] The research reported herein was funded in part by the National Aeronautics and Space Adminstration and U.S. Geological Survey as one phase of the Central Atlantic Regional Ecological Site (CARETS) Project.

[2] Department of Earth Science, University of California, Riverside, Calif.

[3] Department of Geography, University of Wisconsin, Madison, Wis.

[4] Department of Geography, McGill University, Montreal, Canada.

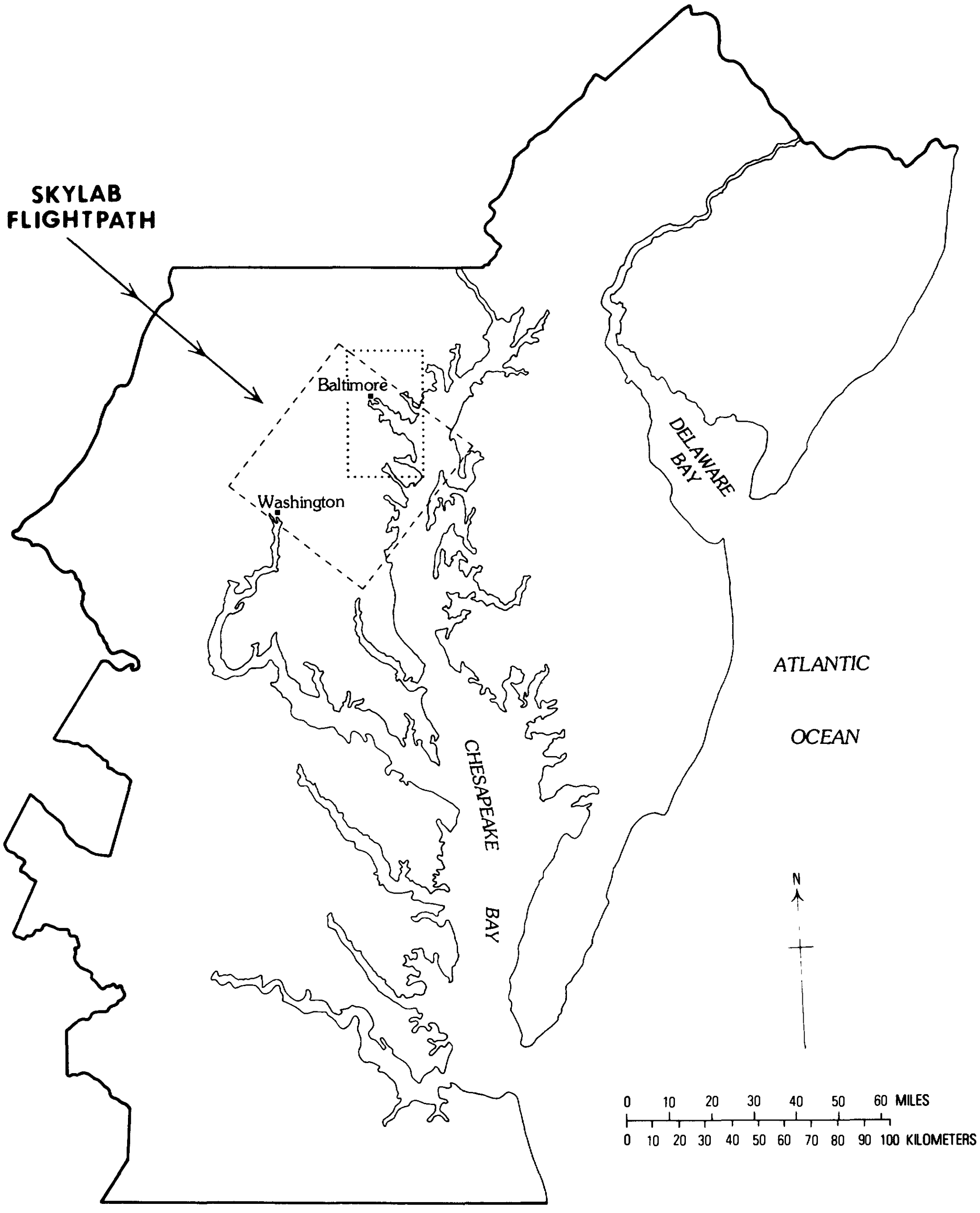

FIGURE 1.—The parts of the Washington-Baltimore area imaged and simulated. The dashed outline delineates the maps of energy-exchange phenomena in this report. The dots outline the area mapped by numerical simulation.

of numerical simulation, using mathematical models of the processes involved. An appropriate name for this avenue of study is "land use climatology."

Currently, there is controversy regarding changes in global climates that result from man's addition of gases and particulates to the atmosphere, but relatively little thought has been given to the goal of this study—the effect on the energy balance of man's manipulation of the Earth's surface. Our concern is not with changes in climate on a global scale, but rather changes at a regional or mesoscale induced by land use. The area of study, which is approximately 6,300 km^2, includes the cities of Washington, D.C., and Baltimore, Md. (fig. 1). Within this area are the two major urban centers, their suburbs, agricultural land, woodland, and the water surface of the upper Chesapeake Bay. The mesoscale of the study does not imply that disruption of energy exchange phenomena on a global scale would have no impact on world climates, but rather that this problem is still to be assessed. The appropriate scale of application at this time is regional. At this scale, the impact of land use and land cover on local climates can be delineated and a concerted response to potential changes can be made.

This paper combines the results of two separate investigations, each with the common goal of energy balance mapping, in order to compare the feasibility and accuracy of the two approaches. One of the investigations uses data gathered by the Earth Resources Experimental Package (EREP) of the National Aeronautics and Space Administration (NASA) Skylab program. The S-192 scanner in the Skylab 3 spacecraft provided information on the thermal state of the Earth's surface in the Washington-Baltimore area at 10:05 a.m. EDT on August 5, 1973. This information was used to construct maps that show the synoptic distribution of surface radiation temperatures, albedos, and net radiation. The other investigation produced maps showing the distribution of energy budget phenomena by use of a general numerical computer model. Linking the results of the two experiments thus demonstrates the potential utility of a combined analysis of the relationship of land use and land cover to local and regional climates.

The two experiments are coupled by place and time. The mapped numerical simulation of surface energy budget data in Baltimore and its environs coincides spatially with a portion of the area mapped with remotely acquired data (fig. 1). Input parameters for the simulated maps match those that existed at the time of the imaging overpass of the Skylab spacecraft, but only to an extent compatible with the independent testing of a general simulation model. Where the model depends upon internal means to determine certain parameters, specific data from the remote mapping experiment were not substituted, in order not to compromise the independence of the general approach.

The initial independence of the two parts of the inquiry is responsible for differences in investigative formats. Most conspicuous is the difference in the size of the data averaging cells—that for the mapping from remotely sensed data is about half the area of that used for simulation mapping. This difference in size affects the comparative resolution of surface detail slightly but does not affect general patterns of distribution, hierarchical orders of values, and the like. In brief, it was felt best to keep each investigation initially independent and then to compare results.

ACKNOWLEDGMENTS

The basic material of this study is derived from chapter 3 of the final report to the Johnson Spacecraft Center for experiment 469 performed by the U.S. Geological Survey (Alexander and others, 1976).

The authors thank Dr. Samuel I. Outcalt of the University of Michigan, author of the Outcalt simulation model, for his counsel in the application of the model for the Baltimore simulation, and thank all others who have contributed to the successful completion of this inquiry.

Appreciation is also extended to Dr. David H. Miller of the University of Wisconsin, Milwaukee, for his critical reading of the manuscript and valuable suggestions that have been incorporated in this paper.

ANTECEDENT STUDIES

Several investigations preceded the inquiries by the U.S. Geological Survey into the remote sensing of surface energy phenomena and the numerical modeling of the energy balance. The following descriptions summarize previous work which led to the present study.

RADIOMETRIC MEASUREMENT BY REMOTE MEANS

The first remote measuring of surface radiation temperatures with an electro-optical scanner were carried out across the island of Barbados, just north of Bridgetown, as part of the Barbados Oceanographic and Meteorological Experiment (BOMEX). The Texas Industries RS-14, one of the first scanners with thermal-infrared capacity and capable of calibration, was used in the experiment as an imaging radiometer (Pease, 1971).

The success of this thermal mapping experiment gave impetus for further experimentation with scanners for measuring surface energy exchange phenomena remotely. The second endeavor was to map a mid-latitude city in the United States (1) to study the heat island effect of cities, (2) to make a series of maps of the surface thermal state to demonstrate diurnal changes, and (3) to map other surface energy exchange phenomena such as surface albedos and the distribution of net radiation. The second mapping experiment, with Baltimore, Md., as the test site city, was designed specifically as a precursor to the Skylab climatology investigation on which this study is based. Three flight lines over the city of Baltimore were imaged at sunrise, midmorning, and early afternoon on May 11, 1972. From the data gathered, maps of the heat island buildup were constructed. Maps showing the distribution of energy emitted by the surface, surface albedos, energy absorbed by the surface, and the distribution of net radiation were constructed for the flightpath across the heart of the city in the early afternoon (12:45 p.m. EST).

The BOMEX and Baltimore missions employed scanners in low-flying aircraft. Spatial perspectives were therefore limited to flightpath swaths approximately 2 km wide. The opportunity to employ a broader perspective by using a satellite came with the NASA Skylab program. Earlier scanners also could not be calibrated to the surface radiance because their electronic circuitry employed automatic gain control (AGC). The gain of these instruments changed with each scanline to keep the dynamic range of values within the sensitometric range of the film on which the image was initially recorded by a cathode ray tube. Three subsequent improvements permitted the RS-14 used in the BOMEX experiment to be calibrated to the surface radiance: (1) the replacement of automatic instrument gain with constant gain which made image elements from various parts of the scanpath comparable; (2) internal calibration sources, the radiances of which were recorded along with the scan image, provided a means for converting the diverse voltage pattern of the image to a radiance pattern with absolute values; and (3) the image pixel information was recorded directly onto magnetic tape which could handle the wide range of values produced when the instrument gain was held constant.

The BOMEX experiment gave the first insight into the problems of calibrating the radiant signals received at the scanner with the signals actually emitted by the terrestrial surface. It was discovered that an airport runway, which measured 52°C radiometrically at the surface, measured only 40°C from an altitude of 300 m. Even though the thermal-infrared sensing was in the so-called "water vapor window," the atmosphere in the optical path to the instrument severely dampened the surface-emitted signal. To circumvent this poorly-understood problem, a target-type calibration of the scanner was employed. Several contrasting targets, of sufficient size to be measured densitometrically on a photographic film image made from the magnetic tape, were measured radiometrically at the surface and plotted against the corresponding film transmittance. The curve produced in this manner matched the sensitometric curve of the film used for photo image printout. From this curve, image transmittances were converted to corresponding values of radiant emission and radiation temperature (Pease, 1971, p. 504).

At the same time it was perceived that the alteration of surface radiant emission followed a gray-window model wherein the air in the optical column attenuated the surface signal as a function of air transmissivity in the sensing spectral band, and at the same time added its own emitted radiation to the weakened surface signal. An apparent reduction in signal strength occurs when the air, cooler than the surface, attenuates more than it emits. The following relationship was established theoretically:

$$I_z=\epsilon[E_{bb}(\overline{T}°K)]+(1-\epsilon)I_0, \tag{1}$$

where I_z is the radiant energy received aloft, ϵ is the emissivity of the air column, $[E_{bb}(\overline{T}°K)]$ is the blackbody equivalent of the radiance of the air column for the mean column temperature $\overline{T}$ in degrees Kelvin, and I_0 is the radiant signal emitted by the Earth's surface. With an accurate knowledge of the radiance values received at the scanner and of the meteorological characteristics of the optical path between surface and sensor, a calibration of the scanner with the thermal-infrared emission of the surface could be made without calibration targets. Although known to be theoretically possible, this type of calibration was not made until the Skylab inquiry described in this paper.

To construct maps for other than the simple thermal state, it was necessary to record simultaneously both Earth-emitted thermal-infrared imaged information and shortwave or reflected solar radiation. This need dictated the use of a calibrated multispectral scanner, and the M-7 scanner of the Environmental Research Institute of Michigan (ERIM) was chosen for the Baltimore experiment. Calibration of the three spectral bands of the multispectral M-7 scanner was done using target values and was performed in the same manner as for the single channel in the BOMEX equipment.

Imaged data from the BOMEX and Baltimore missions were retrieved densitometrically from film transparencies made from magnetic tapes. The size of the data-averaging cell on the image transparency was the size of the aperture of a custom-fabricated densitometer. For the initial BOMEX experiment, a simple densitometer was fabricated by using an adjustable light source, a silicon cell behind a relatively large aperture, and a measuring meter. To preserve the integrity of the matrix of cells, transparent acetate was ruled in a grid with a line spacing that produced squares of the same size as the densitometer aperture. This grid was placed over the film image transparency to give an *x-y* location to values as film transmittances were measured.

For the images from the Baltimore mission, a more sophisticated wide-aperture densitometer was fabricated and placed in the cursor position on an *x-y* digitizer, with the integrity of the grid-cell matrix maintained by the quantizer display of the digitizer. Accurate registration of matrix cells was particularly important because two or more image matrices were necessary to construct maps of surface albedos, energy absorbed by the surface, and net radiation (Pease and Nichols, 1976).

In working with the Baltimore data, ERIM showed that the mapping of surface energy exchange phenomena could also be accomplished directly from the scanner magnetic tapes, bypassing the densitometric analysis of film transparencies.

Except for the maps of radiation temperatures, maps constructed for the Baltimore mission required the combination of data from two or three multispectral channels, and experience was gained in ways to accomplish this. For the albedo maps, two shortwave or solar channels were chosen, one on either side of the rapid rise in chlorophyll reflectance that centers on the 0.725-μm wavelength. The wavelengths chosen were 0.58–0.64 μm in the visual band and 1.0–1.4 μm in the near infrared. In the calculation of albedos, satisfactory weights for the reflectances proved to be 60 percent in the visual band and 40 percent in the near infrared (Pease and Pease, 1972, p. 10). A knowledge of the values of surface albedos plus the values of downwelling longwave radiation from the atmosphere permitted calculation of energy absorbed by the surface which, combined with energy emitted, gave net radiation. To obtain the distribution of net radiation, inputs of data from three channels were combined (Pease and Nichols, 1976, p. 1369). The combination of information from separate multispectral channels later became an integral part of the Skylab inquiry.

NUMERICAL SIMULATION IN LAND USE CLIMATOLOGY

More recently, considerable success has been achieved in the simulation of the surface energy balance by computer. Simulation models have been developed for both urban and nonurban conditions. The general approach is based upon the surface energy conservation equation:

$$R_n = H + LE + G, \qquad (2)$$

where R_n is the radiation balance at the terrestrial surface, H the kinetic or sensible heat flux into the atmosphere, LE the latent energy used in evapotranspiration, and G the flux of heat entering the soil. All four terms are described in energy flux density units. With additional terms, such as those for the phase change in snowmelt or the energy used in photosynthesis, the energy conservation equation is considered to be valid over time scales that vary from 1 second on up (Sellers, 1965, p. 101). It is this equilibrium property of the surface energy expenditure system upon which the concept of surface energy balance simulation is based.

The various surface energy balance models, discussed in context in a later section, differ only in parameterization of particular terms, in input requirements, and in assumptions made. The general approach to each, however, is identical. For each of the four components of the energy balance equation, a combination of input boundary conditions and derived quantities expresses the component as a function of surface temperatures. For any given set of conditions, there is only one equilibrium surface temperature which balances the equation.

Outcalt (1971) developed a digital version of an analog model of the energy balance of the Earth's surface created by Myrup (1969). Although Myrup had developed his model primarily for agricultural surfaces, Outcalt revised it to include specific processes associated with urban surfaces. The Outcalt version simplified simulation by substituting terrain parameters related to land use and land cover for the meteorological parameters originally employed. This substitution permitted data to be input by areas as large as several city blocks to simulate conditions on intricate urban surfaces. Outcalt (1972c) demonstrated that his model was reasonably accurate in predicting surface temperatures associated with various land uses by testing it against actual temperatures at two times on August 5, 1970, in Ann Arbor, Mich., and its environs. In all cases, the ranking of thermal values was correctly simulated, and differences between simulated and observed maximum temperatures were within 15 percent of the total temperature range. These results not only contradicted the concept of a monolithic urban heat island but also indicated that (1) surface wetness is largely responsible for thermal contrasts within the heat island in summer, and that (2) the absorption of beam radiation by vertical walls is the most important environmental factor in winter.

LAND USE CLIMATOLOGY

EFFECT OF URBAN AREAS

Cities are commonly called "heat islands" because a combination of architectural forms, extensive paved surfaces, scarcity of growing plants, and combustion of fossil fuels interact to produce higher temperatures than those in surrounding nonurban lands. In a central business district (CBD), most surfaces have low albedos, or reflectivities, to sunlight and thus are good absorbers of solar energy.

If there were no processes by which this energy could enter and be stored by the substrate, temperatures in the daytime would be significantly higher than they are, and the heat island effect would disappear at sundown. But urban substrates have high heat capacities and movement of absorbed energy into the substrate by conduction both lowers heat island temperatures by day and returns the stored heat to the surface during the night, often maintaining the heat long after sundown. Thus, over a 24-hour or diurnal period, the temperatures of urban surfaces and the air immediately above them are the products of both the incoming solar radiation and the physical nature of urban surfaces. In brief, local climates are products of the types of land use and land cover as well as of the solar input.

When land use and land cover is mapped from remotely sensed data, several levels of discrimination of spatial detail are employed (Anderson and others, 1972 and 1976). A Level I discrimination separates urban and rural categories, and the city, due to land use and land cover thermal intractions, may indeed appear as a monolithic hot spot. A Level II discrimination separates business districts, with their omnipresent hard surfaces, from residential areas in which planted areas act as energy sinks to produce cooler temperatures. A Level III discrimination separates high-density residential areas from low-density areas, the latter with a greater percentage of planted lands in the form of lawns, gardens, and trees, all conducive to lower temperatures. Large parks within a city perform the same function. At this level, a city ceases to be a monolithic heat island and becomes, instead, a mosaic of land use and land cover pieces (polygons), each with its own effect on the air immediately above. Indeed, the concept of a city as a monolithic heat island may be an artifact of obsolete observation methods, like the traditional automobile transecs through urban thermal canyons that do not detect the many surfaces, such as roofs, which are not observable along the route.

The foregoing description suggests that the effect of land use and land cover upon the air above, and thereby on climate, can also be studied at various levels of resolution. These studies may range from the microscale level of a single land use or land cover type, or specific polygon, to the mesoscale level of a large area that may include several cities and any intervening agricultural and wild lands. The multispectral scanner has lifted the level of inquiry from the microscale perspective possible with low-flying aircraft, to the mesoscale perspective possible with a satellite-borne scanner. The scale for studying the dynamics of the urban heat island falls somewhere between these two extremes but is a scale at which the mosaic of differing land use types can be discriminated.

The following is a practical example of the use of this type of information. According to the laws of atmospheric thermodynamics, a city functioning as a heat island would be under an air layer slightly lower in mass atmospheric pressure than the surrounding rural air, causing inward air flow toward the hot core on calm days. Aerial effluents from heavy industries, sewage treatment plants, and the like, placed according to tradition on the east side of the city in our westerly wind belt, may engulf the city under conditions of a stagnant boundary layer. This situation could occur regardless of the location of industry with respect to the city center, when regional wind velocities are low. If cooler types of land use and land cover were distributed throughout the heat island core, these thermally induced pollution diffusion patterns could be changed.

Understanding the factors which control local winds during pollutant-concentrating meteorological conditions may help man manipulate spatial variables that affect local climate. For example, informed placement of heavy industries or activities with potential disaster risks could benefit environmental quality without sacrificing economic use of the land. The ability to observe and simulate the magnitudes and directions of local and regional surface thermal gradients will help achieve these land use planning goals. The ability to observe and map energy phenomena more sophisticated than simple thermal contrasts will also provide insight into the nature of inputs into terrestrial surface energy systems.

METHODS OF OBSERVATION

Earlier efforts to analyze the climatic effect of land use and land cover types, especially urban, were hampered by inadequate methods of observation. Too few observational sites were employed and data were averaged over unnecessarily long times. Synoptic observations, from which an understanding of the dynamics of energy exchange phenomena of the Earth's surface can be developed, have been almost impossible to obtain except by inadequate automobile transects. New methods are needed to study the dynamics of the complex surface energy relationships.

A calibrated electro-optical scanner, whether airborne or spaceborne, acts as an imaging radiometer which can measure the distribution of energy exchange phenomena over a large area in a few moments. If the scanner is multispectral, the information it supplies can be used not only to measure and map synoptic patterns of surface thermal state but also surface albedos, the energy absorbed by the surface, and the distribution of net radiation at the surface. Net radiation is the balance between the energy absorbed by the surface and the energy emitted. If positive in value, it represents energy entering the terrestrial thermal system; if negative a net loss.

One of the problems that has plagued the traditional observer with his array of radiometers on the ground has been the choice for logistic reasons, of sites that represent various surface elements. No single observation site can represent a heterogeneous terrain. Instead, in our method, the scanner substitutes the average value of a matrix cell for the representative site, with the size of the cell appropriate to the ground resolution desired. The system of using a matrix of cells is unequaled in flexibility and accuracy by any ground measurement program because the number of measured points can be as many as the number of image elements (pixels) supplied by the scanner, or fewer when blocks of pixel values are averaged. Ground resolution changes accordingly. The data can be recorded on magnetic tape and transferred directly to digital computers for automated processing without laborious manual preprocessing, or keypunching, into a computer system.

Although calibrated scanline data provide a way to study the diversity of surface energy exchange phenomena as they relate to land use and land cover, these data give no direct insight into the nature of the processes that create the diversity. An analytical tool that can give such insight is a numerical computer model that simulates the processes above and below the Earth's surface and the interaction of these processes across the surface-to-air interface. A model is especially informative about processes if it consists of integrated submodels. These make possible the greatest single value of the energy simulation model, its capability for sensitivity testing. By changing inputs to the model subroutines so as to simulate changes wrought by either man or nature, an investigator can predict effects on the larger integrated energy exchange system.

The model, with its inherent flexibility for the examination of processes by numerical simulation, and the multispectral scanner, with its capability for examining the effects of processes, are two efficient research tools for studying land use climatology. At this stage of experimental development, one acts as a check on the accuracy of the other.

MAPPING OF SURFACE ENERGY BALANCE PHENOMENA FROM SATELLITE-ACQUIRED DATA

Three maps, showing the distribution of phenomena related to the energy balance at the terrestrial surface, were made from data acquired by the S-192 scanner during the Skylab 3 mission. These maps show the distribution of surface radiation temperatures (fig. 2), surface albedos (fig. 3), and surface net radiation (fig. 4). The maps are printed by the GRIDPLOT method where data cells are printed as small squares with pattern densities that indicate relative values. Each cell represented the average value of the radiances of 100 pixels of the scanner imagery and has 10 pixels on each side. We chose this level of averaging or block filtering of information to produce a degree of generalization compatible with the scale of the maps. Each pixel is about 72 m on a side, and each data cell represents a square, 720 m on a side.

Averaging or smoothing data is preferable to attempting to find representative sites. All values of radiance are averaged within each pixel. The mean value of radiance for a 100-pixel block is the average of all individual pixel values in that block. The degree of generalization used for map construction, however, affects the utility of the mapped data as information sources for numerical simulation. Although the simulation model to be described is two-dimensional, it uses point values whereas the data cells mapped from remotely sensed data are 0.72 km on a side. It would appear at first glance that a single pixel (only 72 m on a side) would be a better approximation to a data point than a data cell. Problems arise in using pixels as point data for simulation, however, because the radiance value of a pixel on a magnetic tape is difficult to relate to a surface feature unless the feature is conspicuous.

FIGURE 2.—Distribution of surface radiation temperatures in the Washington-Baltimore area, 10:05 EDT, August 5, 1973. Note prominent heat islands of the two large metropolitan areas. Temperatures less than 25°C are those of clouds. Map is computer-drafted with GRIDPLOT program using 0.52-km^2 data cells.

Scanner-acquired data that have been smoothed or averaged in data cells, on the other hand, can be spatially related to two-dimensional simulation cells with difficulty.

THE S-192 MULTISPECTRAL SCANNER AS A DATA SOURCE

Only the August 5, 1973, imaging pass of the Skylab S-192 scanner provided thermal-infrared

FIGURE 3.—Distribution of surface albedos, Washington-Baltimore area, 10:05 a.m. EDT, August 5, 1973. Albedos greater than 0.25 (white) are those of clouds.

data over the central Atlantic seaboard of sufficient quality to be of use in constructing the energy balance maps. Although this flight path extended southeastward from the Shenandoah Valley across the Delmarva Peninsula, only about one-fourth of the total path was used for mapping. The area mapped (fig. 1) extended from the Potomac estuary to the Chesapeake Bay and included the urban areas of Washington and Baltimore plus a large expanse of semi-urban and nonurban lands to the east and south of these two cities (see larger dashed rectangle on base map). Much of the water surface of the contiguous upper Bay was also included.

The S-192 scanner system has 13 bands, or spectral sensitivities, ranging from 0.41 to 12.5 μm. Thirteen detectors are simultaneously irradiated by

FIGURE 4.—Distribution of surface net radiation, Washington-Baltimore area, 10:05 a.m. EDT, August 5. 1973.

energy from the terrestrial surface, each detector producing an electronic output signal corresponding to the average energy received from the spot on the Earth's surface shown in the scanner system's instantaneous field of view. In the longer wavelengths, the energy consists of the product of the combined radiances of the surface and intervening atmosphere, while in the shorter wavelengths the energy is sunlight reflected by the surface or reflected and scattered upward by the atmosphere. The detector bands and their respective spectral intervals are shown in table 1. Two scan rates were used in the data collection by spacecraft. Subsequent processing of magnetic tapes reduced those data to pixel values.

TABLE 1.—*S–192 detector band coverage*

[Source: NASA/Skylab (1973, p. 3-5); IR is infrared]

Band	Description	Spectral range (μm)	SDO channel
3	Blue-green	0.52–0.56	1,2
4	Green-yellow	0.56–0.61	3,4
5	Orange-red	0.62–0.67	5,6
6	Red	0.68–0.76	7,8
7	Near IR	0.78–0.88	9,10
11	Near IR	1.55–1.75	11,12
12	Near IR	2.10–2.35	13,14
13	Thermal IR	10.2–12.5	15,16,21
8	Near IR	0.98–1.08	19
9	Near IR	1.09–1.19	20
10	Near IR	1.20–1.30	17
1	Violet	0.41–0.46	22
2	Violet-blue	0.46–0.51	18

The S–192 system makes a conical scan which produces a circular scan track of the terrestrial surface and a corresponding scanline on the imagery, skewed moreover by both the simultaneous forward motion of the spacecraft and rotation of the Earth. The angle of the side of the scan cone to the cone axis is 15°. Only the forward 110° segment of the cone is recorded. The scanline can be located with respect to the scanner position, therefore, only by correcting for scan cone and skewness geometry and knowing the altitude, velocity, and track azimuth of the satellite. The imaged path on August 5, 1973, was 69 km wide.

Data from the 13 spectral bands were recorded on 21 of the 28 tracks of the magnetic recording tape as scientific data output (SDO) channels. The relation of the SDO channels to the spectral bands is indicated in table 1. SDO channel 21 (10.2–12.5 μm) was used for the map of radiation temperatures and SDO channel 7 (one of the reflective bands at 0.68–0.76 μm) for the map of surface albedos. The map of the distribution of net radiation was made by combining the information from the two bands with ground and atmospheric characteristics. This project used data from only these two SDO channels.

Data recorded in the spacecraft were Miller-encoded in a pulse code modulation (PCM) form at a density of 16,177.86 bits per inch at a tape speed of 60 in./s. Processing of the scanner tapes after they were returned to Earth in the command module included skew removal, decommutation, conversion to Greenwich Mean Time (GMT), and the production of straight scanlines. The lines were straightened by using pixels from adjacent lines to form a straight sequence across, and at right angles to, the velocity vector of the spacecraft. Since the chord of a circle is shorter than the arc it subtends, the number of pixels in a straightened path is fewer (approximately 1,033) than on a curved scanline (1,240). However, some detail is thereby lost, and individual pixels are not perfectly oriented with respect to the scanpath.

The reformatted tapes were sent to the users by NASA and are the data sources for this project. Digital values are in PCM counts in a hexadecimal code which limits the number of values on each channel of a digitized tape to 255. This number of values for any channel was more than adequate, however, since it considerably exceeded the data spread requirements of the phenomena measured.

In the reformatted NASA tapes, each scanline had its own data block that included pixel values for all channels, plus ancillary information such as latitude and longitude of the first pixel of each straightened line, the location of the spacecraft nadir point at the moment of imaging, and the direction and velocity of the spacecraft. Of the locational information, only the nadir point and first pixel were useful for mapping.

The first step in using the NASA-supplied data was to separate data values for the pixels of discrete scanlines into channel files. In this manner, all pixel data for SDO channel 21, for example, appeared in a single file rather than mixed with other channels in line-by-line blocks. This step consumed the greatest amount of computer time because it required reading all data, much of it useless to the project. The magnitude of the task was reduced by extracting data only from the scanlines needed (1,000 from about 4,000 in the entire scanpath).

CONSTRUCTING THE MAP OF SURFACE RADIATION TEMPERATURES

The method for constructing the map of surface temperatures was the same as that used for all three energy balance phenomena maps. First, data cells were created from the channel pixel files by averaging 10 adjacent pixel values on each of 10 adjacent lines. This produced a smoothing block of 100-pixel values. The data cells were then placed in matrices which yielded the machine-drafted maps (figs. 2 and 4) and the line-printed graymap (fig. 14). Whereas the machine-drafted maps have the planimetry of the scanner-acquired image, the graymaps, on which one line-printed symbol corresponds to one data cell, do not. The graymaps do not have the planimetry of the original image because 10 symbols are typed per inch per line across-track, but there only 8 lines to an inch along-track. This distortion can be corrected by using a 4 × 5 symbol data cell, but the map will be large and unwieldy. A compromise is achieved by using a 2 × 2½ symbol block with two symbols in one line of the cell and 3 in the other.

Although portrayed in hierarchical intervals, each data cell has its own specific value, which is stored for further use. When plotted with a vector line-plotter, contiguous cells within a given interval are joined to form a polygon of given rank, but cell patterns still show conspicuously. One possibility would be to smooth the edges manually to form isarithmic maps. Another possibility would be to apply cell values to cell centroids as control points for automated isarithmic mapping. The number of cells in the maps, however, would demand an excessively large computer memory unless the number were reduced by further smoothing.

The NASA tapes supply data as PCM counts. The equation for converting the PCM counts of SDO channel 21 (thermal infrared) to radiances received at the scanner is:

$$R_z = A_o + C\,A_1, \qquad (3)$$

where R_z is the radiance received aloft in watts per square centimeter per steradian per micrometer (W cm^{-2} ster^{-1} um^{-1}), A_o is a constant equal to 1.3114 ex −4 (1.3114×10^{-4}), C is the PCM count (NASA/Skylab, 1973, p. 5–19) and A_1 is a constant of 4.7650 ex −6. When Chesapeake Bay was used as a substitute calibration target, it was discovered that a correction factor of 1.0513, or approximately 5 percent, was needed to give rational values to temperatures derived by the NASA-supplied equation. For this reason, the conversion equation used was

$$R_z = 1.0513(A_o + C\,A_1). \qquad (4)$$

The rationale for the use of this correction factor will be discussed subsequently.

The form of the radiance (R) used in these equations has a strict definition. Not only is the energy measured in steradians as a measure of radiant intensity, but it is confined to a wavelength interval of 1 μm. This definition arises from the fact that the energy intensity values are for the spectrally narrow sensing window of channel 21 (10.2–12.5 μm) and not for a spectral ban covering all wavelengths. For this reason, the normal $(T°\mathrm{K})^4$ relationship of temperature to the flux of radiation represented by the blackbody curve of the Stefan-Boltzmann equation cannot be used to convert S–192 radiances to radiation temperatures. Because of the manner in which the blackbody curve passes through the sensing window, a temperature-dependent coefficient would be needed that varies from $(T°\mathrm{K})^{4.6}$ to $(T°\mathrm{K})^{5.2}$. The problem is avoided by using the basic Planck equation by which the radiance in any given micrometer wavelength interval can be converted to a radiation temperature and vice versa.

The form of the Planck equation used is based upon wavelength rather than frequency (Hudson, 1969, p. 35). Converted from radiant energy (W_λ) to a radiance (R) by adding π to the denominator, the equation becomes

$$R = \frac{W_\lambda}{\pi} = \frac{c_1}{\lambda^5 \pi} \cdot \frac{1}{e^{c_2/\lambda T°K} - 1}, \qquad (5)$$

where R is the radiance in W cm^{-2} ster^{-1} $\mu\mathrm{m}^{-1}$ for a 1−μm wavelength interval in the sensing window (λ) ; c_1 and c_2 are the first and second radiation constants with values of 3.7415 ex +4 (W cm^{-2} $\mu\mathrm{m}^{-4}$) and 1.43879 ex +4 (μm°K), respectively; T°K is the temperature in degrees Kelvin; and e the natural log base. When all constants are combined, equation (5) becomes

$$R = \frac{0.05921}{e^{1251/T°K} - 1}. \qquad (6)$$

If a temperature is desired from a value of R, the following transposition of equation 6 is used:

$$T°\mathrm{K} = \frac{1251}{\ln \left| \dfrac{0.05921}{R} + 1 \right|}. \qquad (7)$$

Since radiation temperatures provide a convenient common denominator for converting one blackbody expression to another, the conversion of the measured R to this form is an initial step in the data analysis of the thermal-infrared band. The first two steps of this conversion process, then, involve the use of equation (4) followed by equation (7).

Equation (3) converts PCM counts to cgs (centimeter·gram·second) energy units, or W cm^{-2}. The American Meteorological Society stipulates, however, the use of *Système International* (SI) units for climatological work, which expresses energy flows in W m^{-2}, or mks (meter·kilogram·second) units. The current paper accepts NASA data in its cgs form but expresses results in SI units. A certain amount of cross-translation between the two energy expression systems is therefore present which frequently finds common ground in radiometric or radiation temperatures. Although derived from cgs units, the millibar (mb) is retained to describe atmospheric pressure rather than the relatively unfamiliar kilopascal.

THE GRAY-WINDOW ATMOSPHERIC EFFECT

If the R_z received aloft were converted to radiation temperatures, they would portray the surface as being colder than it is. During the August 5 imaging pass, Chesapeake Bay would appear as having had a surface radiometeric temperature of 21°C, whereas its temperature had been measured radiometrically on August 3 as ranging from 26°C to 29°C. This discrepancy arises from the effect of the air in the optical path of the scanner, previously noted as the gray-window model or effect.

The purpose of the following is to restate equation (1) in terms of the R recorded on the NASA tapes. The air absorbs a portion of the surface-emitted radiance (R_0) according to the air transmissivity (T). To the attenuated surface signal is added the radiance of the air column ($R \uparrow a$). Thus, in gray-window theory, there would be no effect by the optical path if the surface temperature and the mean temperature of the air column were the same. The R_0 signal will be damped if the surface is the warmer of the two, and strengthened if it is the colder. This is true because the atmosphere absorbs the same amount of surface-emitted energy as it emits (absorptivity equals emissivity). When warmer than the air, however, the surface emits more energy and thus the amount of energy absorbed by the air will be greater than the amount of energy emitted by the air. Curves for correcting R_z to R_0 approach a line of equal value where $R_z = R_0$ at the mean temperature (or equivalent radiance) of the optical path.

The concept and calculations for the gray-window effect can be simplified for a scanner carried aboard a spacecraft outside the atmosphere. The R_z signal received at the scanner is then composed of the R_0 signal attenuated according to the transmissivity of the intervening atmosphere. To this is added $R \uparrow a$ in the same wavelengths. The simplified relation then becomes

$$R_z = TR_0 + R \uparrow a. \qquad (8)$$

By transposition of this relation, an equation that uses characteristics of the optical path for calibration of the surface radiance to that received by the sensor can be stated as

$$R_0 = \frac{R_z - R \uparrow a}{T}. \qquad (9)$$

By insertion of this equation into the data analysis procedure, the radiance measured by a satellite can be used to derive a surface radiation temperature. The sequence of equations for conversion of SDO channel 21 data to surface radiation temperatures is equation (4), equation (9), and equation (7).

Although the sequence of mathematical manipulation of data appears simple, the derivation of correct values for equation (9) is not. T in the sensing wavelength interval is the product of water vapor absorption residuals in the water vapor window; absorption by aerosols in the air, indicated as atmospheric turbidity; and absorption by gaseous atmospheric pollutants that are nearly transparent. $R \uparrow a$ is the emission of all of these atmospheric components controlled by the emissivity and temperature of the air column.

Complexities in the meteorological analysis of the air column make the use of calibration targets appealing. No targets were prepared for the August 5, 1973 imaging pass. The only water surface, for which temperatures measured radiometrically at the appropriate time were available, was Loch Raven Reservoir north of Baltimore which, unfortunately, was just outside of the imaging path.

Lack of an adequate calibration target on August 5 suggested the desirability of using the surface of Chesapeake Bay as a substitute. This necessitated obtaining temperatures of the bay surface, preferably radiometric, for the appropriate time. The most useful temperatures were those measured radiometrically by the Johns Hopkins University oceanographic vessel, the *Ridgely Warfield*, on August 3, 2 days prior to the Skylab passage. Because of the size of the upper bay, its temperature is considered not to have changed significantly in the 2-day interval. Furthermore, the upper bay is less subject to tidal exchange with ocean water than the lower bay. Because there was a spatial variation in surface readings of from 26° to 29°C, it was necessary to determine an exact relationship between temperatures and PCM counts. To accomplish this, temperatures of the bay surface were mapped with alphanumeric symbols representing PCM counts so that each 100-pixel block was represented by a letter symbol, and a histogram was made of the frequency distribution of the PCM counts (fig. 5). From the map it was ascertained that a PCM count of 149 is equivalent to a surface radiometric temperature of 27°C, or 300°K. It should be noted that the surface of Loch Raven Reservoir, the large body of fresh water north of Baltimore, had a surface temperature of 26.5°C at 10:05 a.m. EDT on August 5. In this manner, Chesapeake Bay provided a calibration target against which the signal modification by the air in the optical path could be checked.

One target, however, cannot provide enough data for converting R_z to R_0. Had two targets been available, the conversion could simply have been accomplished by applying the relation

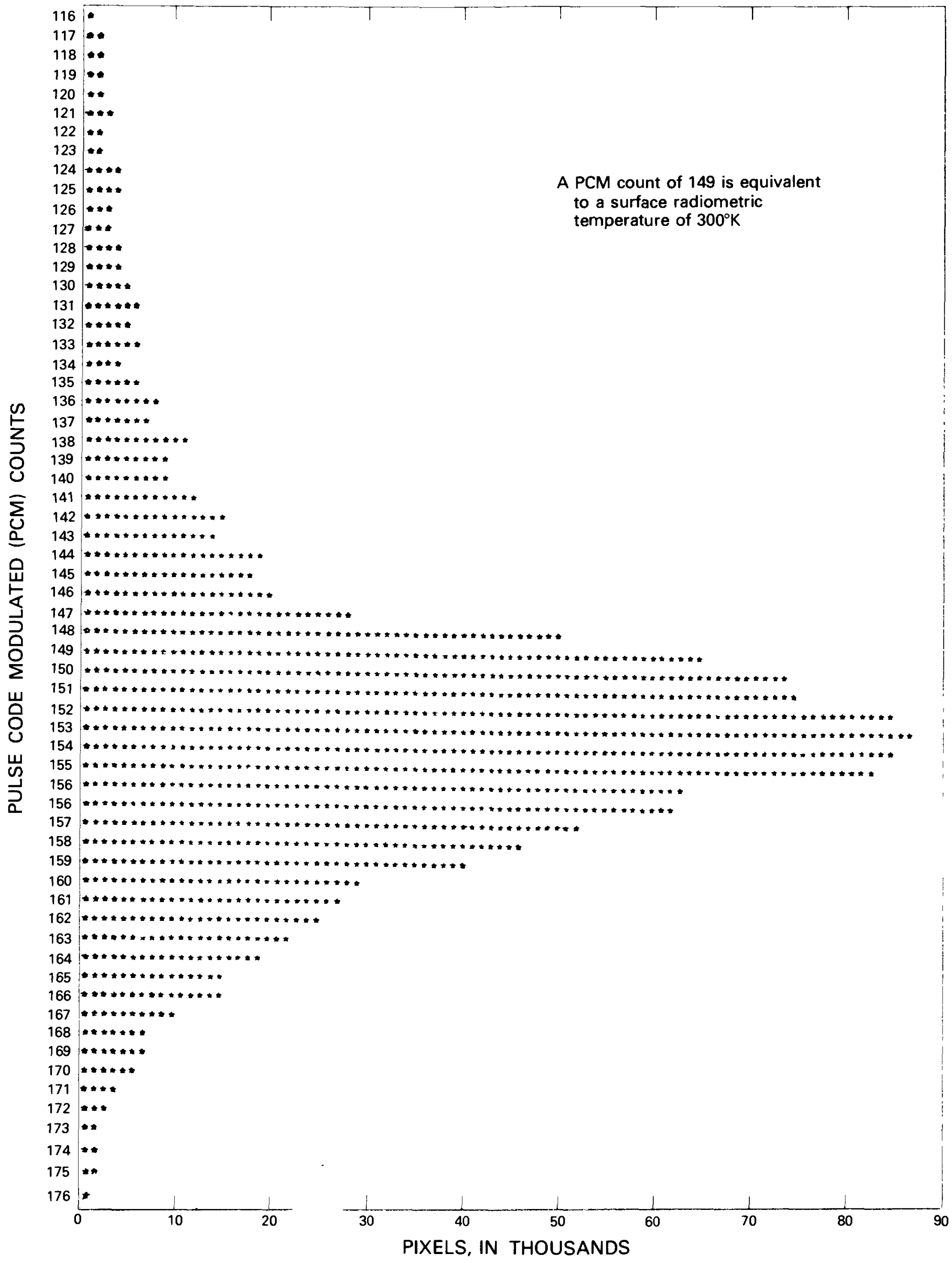

FIGURE 5.—Frequency distribution of pulse code modulation (PCM) counts from scientific data output channel 21 of the S–192 scanner. Data are for the Washington-Baltimore area.

$$T = \frac{R_{zH} - R_{zL}}{R_{oH} - R_{oL}}, \qquad (10)$$

where H and L are subscripts that designate high- and low-radiance calibration targets, respectively. When T, R_z, and R_o are known, $R\uparrow a$ can be found by a transposition of equation (8). The upradiance of the atmosphere is a constant for the calibration values, and the atmospheric correction model provides all of the other values.

CALIBRATION USING CHARACTERISTICS OF THE ATMOSPHERE

The existence of only one valid calibration target for the mapping of the thermal state of the surface, however, forced the use of atmospheric characteris-

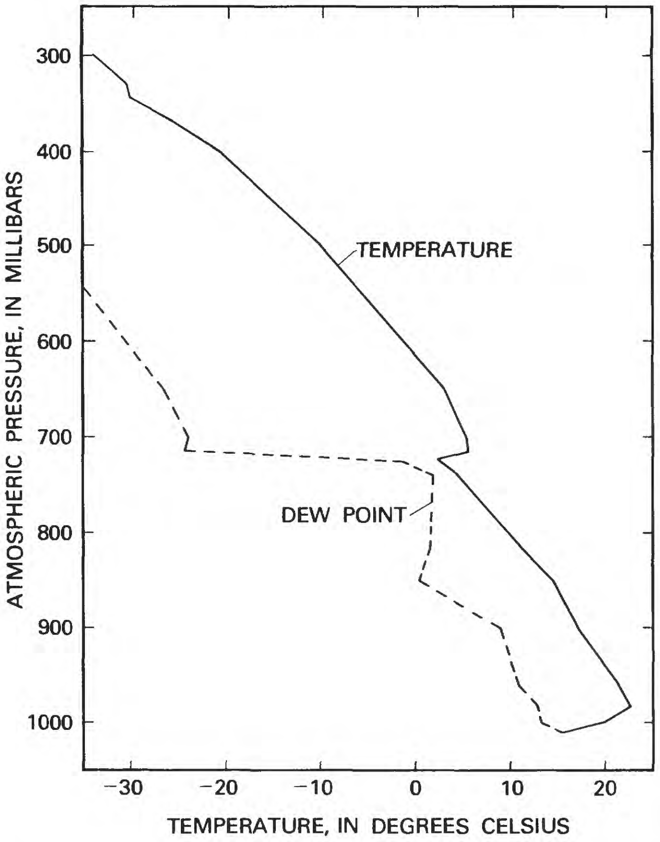

FIGURE 6.—Rawinsonde atmospheric profile, 7:15 a.m. EDT, August 5, 1973, Dulles International Airport, Washington, D.C. Data are from the National Weather Service, Asheville, N. C.

tics to calibrate the sensor to the surface. To accomplish the calibration, it was necessary to determine T in the sensing wavelength interval and $R\uparrow a$ in the same interval. A Rawinsonde profile, made 3 hours before the satellite passage, was then used to determine the water vapor content of the optical path (fig. 6). Although the atmospheric sounding was made at only one point in the imaged area (Dulles International Airport) and represented conditions 3 hours before imaging, the stagnation and apparent homogeneity of the airmass made the record quite usable. Synoptic weather conditions, indicated by both the profile and the daily weather map, consisted of a moist and turbid surface or boundary layer separated from a thick capping layer of dry subsiding air above by a distinct temperature inversion at about 740 mb. Stagnation in the boundary layer is indicated on the weather map by low wind velocities and a high pressure cell over the central Atlantic States. The inversion apparently inhibited, but did not eliminate altogether, the buildup of small and widely scattered *cumulus humilis* clouds. Bands of high *cirrus* clouds extended across Chesapeake Bay in the southern corner of the imaged area (fig. 7).

Water vapor in the optical path acts both as an absorber and emitter of radiant energy between 10.2 and 12.5 μm, even though this spectral band is in the least absorptive part of the 8- to 14-μm water vapor window. Absorption is a function of transmissivity, which is defined in terms of water vapor by the Bouguer-Beers Law as e^{-cw}, where c is a mass absorption coefficient with a value of 0.1 in the 10.2–12.5-μm sensing band (Kondratyev, 1969, p. 119) and w is the water vapor expressed as precipitable centimeters (g cm^{-2}). The value of w can be determined by the following equation:

$$w = \frac{\overline{m}\,(p_2 - p_1)}{g}, \tag{11}$$

where $\overline{m}$ is the mean mixing ratio of the layer of atmosphere in grams of water per kilogram of dry air, $p_2 - p_1$ is the pressure depth of the atmosphere layer in millibars, and g is the acceleration of gravity, 980 cm s^{-2}. The Rawinsonde sounding lists temperatures and dew points as depressions from kinetic (sensible) temperatures for various pressure heights. A pseudoadiabatic chart is the simplest way to obtain mixing ratios, although a form of Teton's equation can be used:

$$\overline{m} \approx q_w = \frac{3798\,(10^{7.5t/T_D+237.3})}{p}, \tag{12}$$

where T_D is the dew point in °C and p is the atmospheric pressure in millibars. The value of $\overline{m}$ is very close to that of q_w, the specific humidity, and for our purposes can be considered the same.

Since upward emission from each small but finite layer of the atmosphere is modified by the layer above through attenuation and additional emission, a high-resolution numerical integration of values upward will yield the most accurate value of $R\uparrow a$ into space. Analysis is more easily accomplished, however, by treating the atmosphere as consisting of a smaller number of layers, particularly when more than one modifying element must be combined at each level (table 2). The water vapor and temperature profile data are tabulated as if the atmosphere were in five layers below the inversion but in a single layer above, because the subsiding air above has low water vapor content and turbidity and thus is relatively inactive as a modifying element. The data for layer 1, that closest to the surface, are at the top of the table 2.

The overall thermal infrared (IR) transmissivity of the profile is calculated by multiplying all discrete

FIGURE 7.—S–192 scanner image of the mapped area. The image is a film print of data from scientific data output channel 7 (band 6), the channel (0.68–0.76 μm) used for mapping surface albedos. The image, a mosaic of information from two sequent tapes, retains the conical linescan format.

layer transmissivities together. For the simple water vapor model described by table 2, the value of T is 0.823. $R\uparrow a$ is calculated by multiplying the upward radiance of layer 1 ($R_1\uparrow$) by the transmissivity of layer 2 (T_2) to which is added the upward radiance of layer 2 ($R_2\uparrow$). This accumulated value is processed through layer 3 in the same manner, and this method is repeated for all layers and into space. The process is shown by the following relationship:

$$R\uparrow a = ((((R_1\uparrow T_2+R_2\uparrow)\,T_3+R_3\uparrow)\,T_4+R_4\uparrow)\,T_5+R_5\uparrow)\,T_6+R_6\uparrow = 1.3534 \text{ ex } -4 \text{ W cm}^{-2}\text{ ster}^{-1}\,\mu\text{m}^{-1}. \tag{13}$$

The subscripts indicate the layer numbers. A calibration model which considers only water vapor modifications is then

$$R_o = \frac{R_z - 1.3534 \text{ ex } -4}{0.823}. \tag{14}$$

Using this model and making the assumption that a PCM count of 149 is the equivalent of 27°C (300°K), the radiation temperature of the hottest data cell in the Baltimore CBD was 39.18°C.

It is apparent from the synoptic meteorological conditions that prevailed during the Skylab 3 pas-

TABLE 2.—*Gray-window analysis of the atmospheric profile, including effects of water vapor only*

[Data source: Rawinsonde profile for Washington, D.C. (Dulles International Airport)]

Range: Pressures at top and bottom of air layer, in millibars.
Depth: Pressure depth of air layer, in millibars.
$\overline{T}$°C: Mean temperature of air layer, in degrees Celsius.
DP°C: Mean dew point of air layer, in degrees Celsius.
$\overline{m}$: Mean mixing ratio of air layer, in grams per kilogram.
w: Water vapor in air layer as precipitable centimeters (grams per square centimeter).
T_{wv}: Transmissivity of air layer containing water vapor.
ϵ: Emissivity of air layer.
$R\uparrow$: Radiance emitted upward from air layer, in watts per square centimeter per steradian per micrometer.

Note: Values for T_{wv}, ϵ, and $R\uparrow$ apply only to spectral band 13, scientific data output channel 21, of the 10.2–12.5 μm sensing window.

Layer	Depth	$\overline{T}$°C	$\overline{DP}$°C	$\overline{m}$	w	T_{wv}	ϵ	$R\uparrow$
1000–950	50	21.64	12.6	9.3	0.474	0.954	0.046	3.9563 ex –5
950–900	50	19.28	9.6	8.2	.418	.959	.041	3.4057 ex –5
900–850	50	15.56	5.0	6.2	.316	.969	.031	2.4350 ex –5
850–800	50	11.90	1.3	5.1	.026	.974	.026	1.9302 ex –5
800–740	60	7.15	1.8	5.7	.349	.966	.034	2.3409 ex –5
Inversion—740 mb (2.45 km)								
740–365	375	–12.0	–36.0	.35	.134	.987	.013	.6429 ex –5

sage on August 5 that factors other than water vapor were modifying the surface signal. A meteorological visibility of only 16 km reported at Washington, D.C., on the daily weather map indicated significant atmospheric aerosol density (turbidity), probably associated with urban pollution that accompanies stagnant air conditions. It has been noted in similar synoptic situations that the turbidity becomes fairly evenly dispersed when the stagnant airmass persists for some time. The aerosols remain in the boundary layer because the temperature inversion inhibits vertical motion of lower air into the air aloft. This was observed on two occasions in the summer of 1975 during aircraft departures from Dulles Airport west of Washington. Turbidity disperses upward in the boundary layer, possibly with a slight increase just below the inversion. A homogeneity of atmospheric components in the surface or boundary layer is assumed for this study, however.

Previous work in atmospheric optics by McClatchey and others (1972) as well as by Pease in the eastern end of the Los Angeles Basin in the summer of 1975 indicates that aerosols and gaseous pollutants in a scanner optical path both absorb and radiate between the wavelengths of 10.2 and 12.5 μm. Therefore, during turbid pollution conditions, as apparently existed over the Los Angeles test site at the time of imaging, the effect of aerosols and pollutants must be included in the gray-window calibration model.

Turbid air transmissivity (T_t) in thermal-infrared wavelengths is not the same as in visual wavelengths for the same airmass conditions. In the short wavelengths, the aerosols primarily scatter light. McClatchey and others (1972) indicate that at a wavelength of 0.514 μm and a meteorological visibility (V_m) of 5 km, scattering of light exceeds absorption by a ratio of more than 1:100,000, but at a wavelength of 10.59 μm in the same airmass, absorption will be almost triple the scattering. Several methods exist for ascertaining T_t in the visual wavelength realm, but conversion of this value to a thermal-infrared equivalent is still a problem.

Meteorological visibility is routinely reported with weather observations and can be converted to the visual transmissivity of turbid air (T_{vis}) by either of two methods. One involves the following two steps:

$$(1)\ \sigma_{sw}\,\mathrm{km}^{-1}=3.912/V_m,\ \text{and}\ \ (2)\ T_{vis}\,\mathrm{km}^{-1}=e^{-\sigma sw}, \tag{15}$$

where σ_{sw} is the shortwave scattering coefficient. A second and more direct method is

$$T_{vis}\,\mathrm{km}^{-1}=(0.02)^{1/V_m}. \tag{16}$$

The second method depends upon three facts: (1) that by definition, the value 0.02 is the minimum contrast the eye can detect when a dark object is outlined against the skyline, (2) that contrast under these conditions is interchangeable with transmissivity, and (3) that sequential transmissivities are multiplicative and therefore bear an exponential relation to each other. A meteorological visibility of 16 km becomes a T_{vis} of 0.783 km^{-1} by either method.

A more difficult and less definitive step is the conversion of a visual transmissivity to an equivalent transmissivity in the thermal infrared (T_{tir}), which is an expression needed in a complete atmospheric correction model. There is little in the literature to use as a guide for this process. On the basis of Mie theory, as expressed by McClatchey and others (1972), the ratio of extinction coefficients between the 0.51-μm and 10.5-μm wavelengths is 0.082. T_{tir} can then be expressed as $(T_{vis})^{0.082}$. The term "extinction coefficient (γ)" is used here to include the sum of both absorption and scattering coefficients. In figure 8, extinction coefficients for a thermal-infrared wavelength of 10.591 μm are plotted against meteorological visibilities ranging from 5 to 23 km. Use of this translation of visual to longwave turbidity transmissivities for the August 5 imaging gives a T_{tir} of 0.980 km^{-1}: 0.952 for the entire boundary layer below the inversion, or about 0.990 for each of the 50-mb layers in the profile calculations. Although T_{tir} modifies the surface signal less than water vapor ($T_{wv} = 0.823\ \text{km}^{-1}$), T_{tir} nevertheless is a factor to be considered in the calibration.

A calibration model which incorporates both water vapor and turbidity effects, based upon the above value of T_{tir} is

$$R_o = \frac{R_z - 1.712 \text{ ex } -4}{0.7884}. \qquad (17)$$

The ratios of thermal-infrared (10.59 μm) to visual extinction coefficients ($\gamma_{tir}/\gamma_{vis}$), obtained by observations within the Los Angeles Basin in summer, are on the same order as the values obtained by the Mie theory at times when turbidity consists only of moisture haze or evaporating fog. When these conditions prevail, ratios that range from 0.05 to 0.10 have been empirically ascertained. These ratios compare favorably with the ratio of 0.082 derived from the work of McClatchey and others (1972). Under conditions where smog pollutants are prevalent, however, the ratio rises rapidly and approaches 1.0.

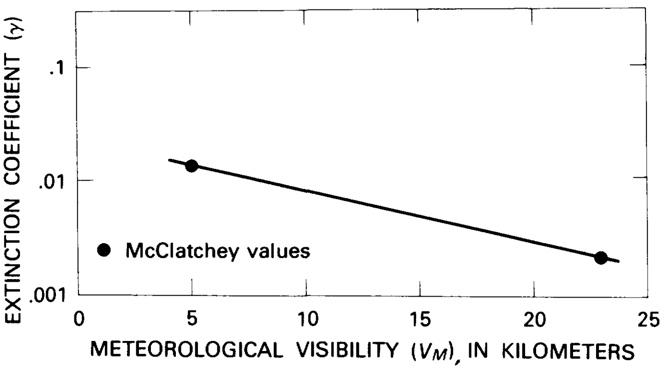

FIGURE 8.—Extinction coefficients (γ) at a wavelength of 10.591 μm, for various visibility ranges (McClatchey and others, 1972).

This high value is taken as evidence that gaseous pollution can be a significant factor in the gray-window effect. When mixtures of aerosol haze and gaseous pollution exist, ratios of γ_{tir} to γ_{vis} commonly range from 0.20 to 0.50 with 0.30 being a typical value for moisture haze that contains a moderate amount of gaseous pollution. This finding agrees with Yates and Taylor (Wolfe, 1965, p. 206–210) for summer measurements along horizontal paths over Chesapeake Bay, for which a typical ratio was 0.30.

Spectrometric analysis of common smog gases supports the assumption of pollution effects. Although the strong absorption band of ozone (9.6 μm) is outside the sensing waveband, several minor constituents (for example, propylene and ethylene) have minor absorption-emission bands within the sensing band. Peroxyacetyl nitrate (PAN), a persistent smog gas and one of the most prevalent where pollution is derived from automobile exhausts, has strong absorption-emission characteristics between 10 and 12 μm (fig. 9). For the gas concentrations for which the curve was prepared, transmission in the thermal-infrared sensing band is only 74 percent, which suggests a significant gray-window effect.

Use of the 0.30 extinction coefficient ratio converts the 0.78 km^{-1} visual transmissivity of August 5, derived from the meteorological visibility at Washington, D.C., to an equivalent T_{tir} transmissivity of 0.93 km^{-1} or $(0.78)^{0.3}$. This value translates to approximately 0.965 per 50-mb layer. An analysis of the optical path over the imaging site, which includes the turbidity-pollution factor, is presented in table 3. For each layer, the value of T_{wv} from table 2 is multiplied by the T_t derived from the depth of the layer in fractions of a kilometer and the 0.3 coefficient, to obtain the overall transmissivity ($T_{wv,t}$) of the layer. Multiplication of all layer transmissivities gives a value of 0.6925 for the entire atmospheric column in the sensing waveband.

As shown in table 2, the $R\uparrow$ from each layer is attenuated by the transmittance of the layer above, and so forth, to the top of the atmosphere. The values of $R\uparrow$ in the extreme right-hand column of table 3, however, are based on the sum of the effects of water vapor, aerosols, and gaseous pollutants emission, and the total emissivity of the layer ($\epsilon = 1 - T$) with respect to these three elements and its Kelvin temperature. The $R\uparrow a$ recorded by a satellite-borne scanner is 2.4097 ex −4 W cm^{-2} ster^{-1} μm^{-1}. From this value, a conversion

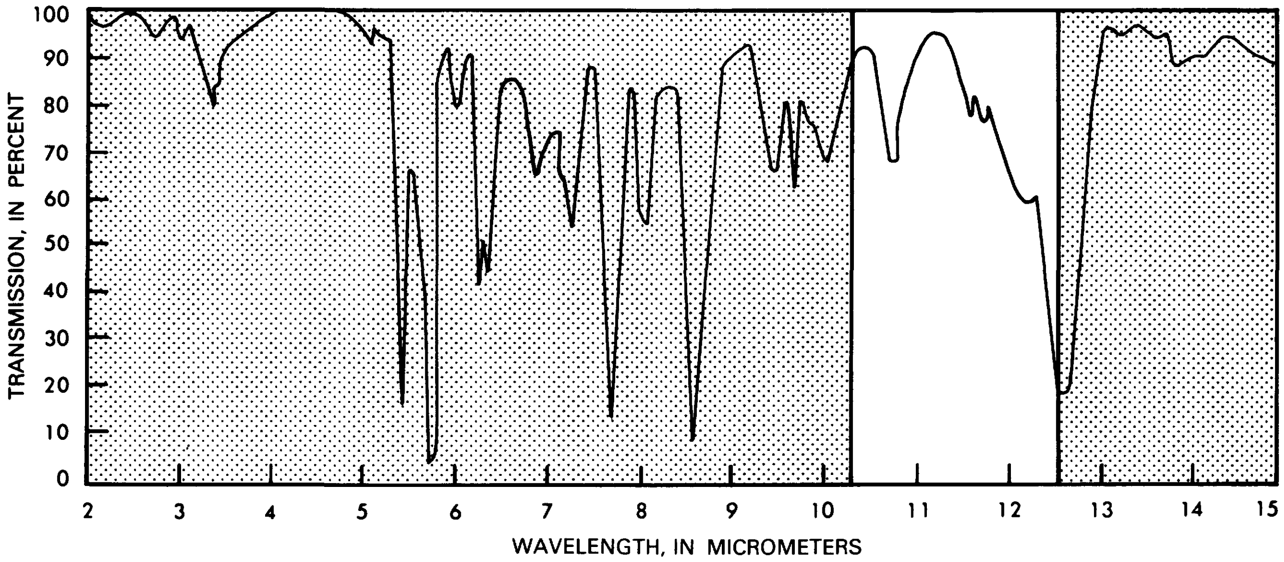

FIGURE 9.—Absorption spectrum of peroxyacetyl nitrate. The non-shaded area is the 10.2- to 12.5-μm sensing window of thermal-infrared scientific data output channel 21 of the S-192 scanner (Scott and others, 1957).

TABLE 3.—*Gray-window analysis of the atmospheric profile, including effects of water vapor, aerosols, and gaseous pollutants*

[Data source: Rawinsonde profile for Washington, D.C. (Dulles International Airport) 1115 GMT (7:15 a.m. EDT) August 5, 1973]

Air layer bottom to top: Pressure in millibars and elevation in kilometers.
Air layer depth: Pressure in millibars and thickness in kilometers.
T_{wv}: Transmissivity of air layer containing water vapor.
T_t: Transmissivity of air layer containing aerosols and gaseous pollutants.
$T_{wv,t}$: Transmissivity of air layer containing water vapor, aerosols, and gaseous pollutants.
ϵ: Emissivity of air layer.
$R\uparrow$: Radiance emitted upward from air layer, in watts per square centimeter per steradian per micrometer.

No.	Air layer				Water vapor			Aerosols and gaseous pollutants			Water vapor, aerosols, and gaseous pollutants	
	Bottom-top		Depth									
	mb	km	mb	km	T_{wv}	ϵ	$R\uparrow$	T_t	ϵ	$R\uparrow$	$T_{wv,t}$	$R\uparrow$
1	1000–950	0–0.42	50	0.42	0.954	0.046	3.9563 ex −5	0.969	0.031	2.6659 ex −5	0.924	6.6221 ex −5
2	950–900	0.43–0.85	50	0.42	0.959	0.041	3.4057 ex −5	0.966	0.034	2.8242 ex −5	0.928	6.2299 ex −5
3	900–850	0.86–1.32	50	0.46	0.969	0.031	2.4350 ex −5	0.966	0.034	2.6706 ex −5	0.936	5.1056 ex −5
4	850–800	1.33–1.82	50	0.49	0.974	0.026	1.9302 ex −5	0.963	0.036	2.6726 ex −5	0.939	4.6028 ex −5
5	800–740	1.83–2.45	60	0.62	0.966	0.034	2.3409 ex −5	0.963	0.037	2.5474 ex −5	0.931	4.8883 ex −5
Inversion—740 mb, 2.45 km												
6	740–365	2.46–8.21	375	5.75	0.987	0.013	0.6429 ex −5	----	----	-----	0.987	0.6429 ex −5
								Total for entire atmosphere			0.6925	2.4097 ex −4

equation for surface radiation taking a vertical path through the atmosphere to the sensor is

$$R_o = \frac{R_z - 2.4097 \text{ ex } -4}{0.6925}. \tag{18}$$

The equation used to make the map of surface radiation temperatures (fig. 2) was corrected for the 15° slant path of the conical scan pattern of the S–192 scanner and is:

$$R_o = \frac{R_z - 2.4947 \text{ ex } -4}{0.6835}, \tag{19}$$

but values from either equation are similar. The procedure for converting PCM counts of SDO channel 21 to radiation temperatures in degrees Celsius is given in table 4.

To corroborate the values of T and $R\uparrow a$ used to compute equation (19), a day was chosen in which a mixture of moisture haze and pollution in the eastern end of the Los Angeles Basin represented the mixture in the boundary layer through which the Skylab scanner imaged on August 5 over the Washington-Baltimore area. The day was July 24, 1975, and the site was near the city of San Bernardino where atmospheric soundings were being made by the Forest Fire Laboratory of the U.S. Forest Service. Downward longwave radiation between 10 and 12 μm was measured with a Barnes PRT–5 radiation theromometer. After corrections were made to the San Bernardino data for the difference in depth, temperature, and atmosphere profile between the

TABLE 4.—*Procedure for converting pulse code modulation (PCM) counts to temperature in degrees Celsius ($T°C$)*

[If a model other than the urban model described is desired, substitute different values based on $R\uparrow a$ and T for the constants in step 2 and alter conversion factor appropriately]

Step 1.	Convert PCM count to R_z: $R_z = 1.0513(A_0 + C\,A_1)$.	where: R_z=radiance received at scanner in W cm^{-2} ster^{-1} $\mu\mathrm{m}^{-1}$, 1.0513=correction/matching factor, A_0=1.3114 ex −4, C=PCM count, and A_1=4.7650 ex −6.
Step 2.	Convert R_z to R_0: $R_0 = \frac{R_z - 2.4947 \text{ ex } -4}{0.6835}$.	where: R_0=radiance at surface in W cm^{-2} ster^{-1} $\mu\mathrm{m}^{-1}$.
Step 3.	Convert R_0 to $T°K$: $T°\mathrm{K} = \frac{1251}{\ln\left\lvert \frac{0.05921}{R_0} + 1 \right\rvert}$.	where: $T°K$=temperature, in degrees Kelvin.
Step 4.	Convert $T°\mathrm{K}$ to $T°\mathrm{C}$: $T°\mathrm{C} = T°\mathrm{K} - 273$.	

turbid layers at the two sites, the down-radiance at San Bernardino was computed to be 2.4397 ex −4 W cm^{-2} ster^{-1} $\mu\mathrm{m}^{-1}$. This compared well with the value of $R\uparrow a$ used in equation (19). Calculations using atmospheric profile data show that downward longwave radiation measured at the surface is essentially the same as upward longwave radiation at the top of the atmosphere.

Because of the uncertainty in the accuracy of the corrections made for gaseous pollution and turbidity, the differences between the three conversion models were determined by using each to calculate a surface radiation temperature for a high PCM count (PCM=176). It was assumed that a PCM count of 149 is equivalent to a surface radiation temperature of 27°C. For each of the following equations, a PCM count of 176 is equivalent to the following temperatures:

Equation 14:
  water vapor only =39.18°C
Equation 17:
  water vapor + aerosols =40.14°C
Equation 19:
  water vapor + aerosols
  + gaseous pollutants =41.30°C

The difference is not great, but logic demands the most complete and accurate answer.

THE NEED FOR A DATA-CORRECTION FACTOR

As previously stated, a correction of about 5 percent was made in the conversion of PCM counts to radiances. When the PCM count of 149 matches a radiation temperature of 27°C, as occurred on August 5 on the surface of Chesapeake Bay, no choice of transmissivity will yield an upradiance sufficiently large to match the radiance calculated from the atmospheric elements in the optical path. This problem is not simply due to an incorrect choice of model values, because the upradiance is considered a function of the transmissivity of the active atmospheric layers in the column and because emissivity is the unity complement of the transmissivity ($\epsilon = 1 - T$). To satisfy the emissivity-transmissivity relationship without the correction factor, the temperature of the bay would have to be near 21°C, far colder than was measured radiometrically from the *Ridgely Warfield*. The upradiance is also a function of air temperature, but, again, a much colder air than was present would be necessary to permit a true transmissivity-emissivity relationship without the correction factor.

The correction factor used was obtained by calculating a value of R_0 that matched 27°C (300°K), using equation (6). A corresponding value for R_z was calculated with equation (8). The factor is then

$$\text{Correction factor} = \frac{R_z \text{ (calculated)}}{R_z \text{ (NASA supplied)}}. \qquad (20)$$

A physical basis for this apparent discrepancy between spacecraft-acquired radiance values and the gray-window calibration may be due to the scattering of the sensed surface signals by aerosols in the optical path. Whereas signals absorbed by these particles will be replaced by particle emission, photons scattered out of the optical path may have no replacements. Loss of radiant energy without replacement would cause the transmissivity of the air column to be less than the unity complement of the emissivity.

There has been too little investigation of the nature of scattering of longwave (10-μm) radiation by typical aerosol populations. Workers in the field have been prone to ignore scattering when clouds are not present (Kondratyev, 1969, p. 558). Water vapor has been assumed to absorb but not scatter radiation of these wavelengths. McClatchey and others (1972, p. 24) indicate, however, that radiation at a wavelength of 10.591 μm is about equally absorbed and scattered by typical aerosol populations, a fact that gives scattering some significance when the gray-window model is used to calibrate scanners sensing through turbid paths.

One can make a case for a condition in which any solid or liquid particle in the air of the optical path can deflect off-axis photons toward the sensor and in this way replace on-axis radiation lost by scattering. This radiation would not have originated at the point being imaged, however, nor would the radiation strength be tied to the emissivity and temperature of the air column as is the case in aerosol emission.

The directional nature of aerosol scatter of 10-μm radiation is also poorly understood. More than 95 percent of most aerosol populations, other than clouds and fog, are particles with radii of 1.0 μm or less (Junge, 1963, p. 117). Since this dimension is less than one-tenth the wavelength of the sensing radiation, moderate Rayleigh scattering should exist and considerable omnidirectional scatter should take place. Rayleigh scatter by a particle with a 1-μm radius bears about the same relation to 10-μm radiation as scatter by a particle in cigarette smoke does to visible light. For particles in the population with still smaller radii, Rayleigh-type scatter would be even stronger. In the case of omnidirectional scatter, surface-emitted on-axis radiation should have about the same chance of reaching the sensor, after scattering, as aerosol-emitted radiation, a condition favoring the unity complement relationship of the emissivity and transmissivity of the optical path.

Many of the particles in aerosol populations over urban centers are opaque and, considering the ratios of their sizes to the sensing wavelengths, should predominantly backscatter by reflection (Kondratyev, 1969, p. 182). The degree of backscatter, however, depends upon the reflectivity of the particle and probably would be less than 10 percent of the incident radiation with a 10-μm wavelength. The remainder of the radiation would be absorbed. Diffraction scatter of the surface signal being imaged, although strongly forward, would still be deflected away from the sensor.

It is clear that scatter of the longwave radiation by aerosol populations in the scanning optical axis may create uncertainty in the gray-window calibration. The correction factor described may be a pragmatic and empirical solution to the problem of uncertainty, but a solution which necessitates a surface calibration target, such as Chesapeake Bay provided for this investigation.

CONSTRUCTING THE MAPS OF SURFACE ALBEDOS AND NET RADIATION

When the map of surface albedos (fig. 3) was made, the gray-window calibration of the scanner sensor to the surface was not used because no adequate model for handling the effects of the scatter of shortwave or solar light had been developed. A calibration approach was used in which natural surfaces, the albedos of which are well known, acted as surrogates for targets measured specifically for the inquiry.

Because albedo values are fairly conservative when measured for specific conditions, such as the seasonal state of vegetation, contrasting targets of known albedo were used. For the low end of the reflectance range, the water surface of Chesapeake Bay was chosen. Deep water with low turbidity and few waves has an albedo of about 2 or 3 percent. A value of 2.5 percent was given to the darkest water surfaces of the bay under cloud-free conditions. For the high end of the albedo range, fields with bright herbaceous or grass cover were chosen, and these were given an albedo value of 22 percent, which is typical for bright vegetated surfaces in the summer. The 22-percent albedo value matches measurements made in Baltimore in May 1972 by the authors, and is supported by the work of S.R. Pease and R.W. Pease (1972, p. 21), and Sellers (1965, p. 21). As an intermediate target value, an albedo of 10 percent was assigned to the CBD of Baltimore (Pease and Nichols, 1976, p. 1369).

A spectral sampling technique was employed to measure surface albedos with the S-192 scanner, rather than a technique that attempted to measure all reflected sunlight. Integration of information from all shortwave scanner channels would require extensive computer time and be prone to errors that arise from the weighting of a number of channels with overlapping wavebands. Dirmhirn (1968) determined that spectrally selective sensors are feasible for measuring albedos if they sample on either side of the rapid rise in plant reflectance that centers at a wavelength of 0.725 μm. Two bands are used, one sensing at wavelengths shorter than and the other at wavelengths longer than this critical point. Weighting of the results was based on the wavelength distribution of sunlight, 60 percent in the shorter wavelengths and 40 percent in the longer (Pease and Pease, 1972, p. 7). One band can be used if it straddles the midpoint with a sensitivity that matches the 60/40 weighting. Although spectrally narrow, the sensitivity of the S-192 band 6 (SDO channel 7) of 0.68 to 0.76 μm has this weighting and has been used singly to determine albedos. Vegetation was the critical surface sampled. Other surfaces, such as blacktop, water, and a generalized CBD surface, have monotonic reflectance curves that change gradually and uniformly and, for them, the narrow sample suffices well.

Because the relationship of PCM counts to the radiances they represent is linear, because a target-type calibration was used, and because the final product does not represent an energy value, no conversion was made from PCM counts to radiances. Rather, the count numbers for the calibration targets were plotted directly against the albedos they represented to create a conversion curve.

Several cells with albedos higher than 25 percent are present on the map (fig. 3). These light spots are clouds and land classified as disturbed or transitional, which typically may reflect more than 50 percent of the sunlight. One cloud shadow west of Baltimore appears as an area of low albedo. On a map of surface albedos, made from information acquired above the cloud level, clouds produced unwanted spectral noise, but no attempt was made to remove it.

Procedures for constructing the albedo map are listed in table 5. The construction of maps of surface albedos and net radiation is not the major interest of this inquiry, which is to compare the thermal state of the surface measured by remote means with that determined by simulation. These maps were made, however, to demonstrate the feasibility of measuring spatial patterns of energy exchange phenomena requiring the combination of information from two or more bands of a multispectral scanner in a spacecraft.

Each 100-pixel cell of the net radiation map not only includes a radiation temperature and albedo information but also solar input and atmospheric downradiation data.

TABLE 5.—*Procedure for constructing an albedo map of the Washington-Baltimore area*

1. Create a file of SDO channel 7 PCM counts.
2. Block filter this file into 100-pixel cells (10 adjacent pixels on 10 adjacent lines) and average the pixel values within each cell.
3. Make a histogram of the values of the block-filtered cells. This histogram will show a trimodal distribution: low values for Chesapeake Bay, an intermediate grouping for land reflectances, and a small high-value group for cloud reflectances.
4. Assign the lowest PCM counts of the lowest count group an albedo value of 0.025 (2.5 percent).
5. Assign the highest PCM counts of the intermediate group an albedo value of 0.22 (22 percent).
6. Create a curve based on PCM counts plotted against albedos. This curve will be a straight line between the two plotted points.
7. Write a linear equation for the curve.
8. Create a plot tape of albedo values that correspond to the cells of the matrix.
9. Enter the hierarchy of value intervals into the plotting program: for example, 0.05 (5-percent) intervals.
10. Plot map by:
    - a. Line-printed cells for graymap (2- × 2.5-symbol spacing),
    - b. Machine-drafted grid-cell plot as in figure 3, or by,
    - c. Contouring data, if memory capacity of computer permits it. Additional block filtering is suggested if isarithmic maps are desired.

To calculate the radiation balance for each data cell, the radiation temperature must first be converted to energy emitted by the surface ($E\uparrow$) by the use of an appropriate form of the Stefan-Boltzmann equation, (5.678 ex −8) $(T°K)^4$, with energy in watts per square meter. Determination of energy absorbed by the surface ($E\downarrow$) is more complex. Incoming solar radiation, both beam (Q) and diffuse (q), is multiplied by $(1-a)$, where a is the albedo, to find the solar energy absorbed. The value for incoming solar radiation, measured with a pyranometer at Loch Raven Reservoir at the time of the satellite overpass, was 859 W m^{-2}. Based on the assumption of a homogeneous boundary airmass, this value was used for the entire area mapped. Because no measurement was made of the downward longwave atmospheric radiation at the same time, a value was estimated by use of an empirical equation by Brunt, as restated by Kondratyev (1969, p. 572):

$$G_0=\sigma T_z^4\,(a_1+b\sqrt{0.751P_v}), \qquad (21)$$

where G_0 is the downward longwave radiation in W m^{-2}, σ the Stefan-Boltzmann constant of 5.678 ex −8, T_z the temperature at screen height (approximately 1.8 meters above the ground) in degrees

Kelvin, P_v the vapor pressure in millibars, and a_1 and b are empirical constants of 0.55 and 0.056, respectively. When all constants and a vapor pressure of 16.71 mb are entered, the equation becomes

$$G_o = 0.74\,\sigma T_z^4. \tag{22}$$

The net radiation (R_n) for each data cell becomes

$$R_n = E\downarrow - E\uparrow = \epsilon\sigma T_o^4 - [0.74\,\sigma T_z^4 + (Q+q)(1-\mathrm{a})], \tag{23}$$

where ϵ is an emissivity of 0.95, T_0 the temperature of the Earth's surface in degrees Kelvin, $Q+q$ the incoming solar radiation in watts m^{-2} and a the albedo derived from figure 3.

The accuracy of the net radiation map (fig. 4) is only as good as the accuracy of the albedo map. Values computed, however, appear reasonable considering the humid conditions of the boundary layer which inhibited evaporation from Chesapeake Bay and evapotranspiration of vegetated areas. Loss of absorbed energy by evaporation during daytime hours is the prime cause of a positive net radiation balance.

MAPPING BY NUMERICAL SIMULATION

Numerical modeling of the planetary boundary layer and interface has progressed significantly since the early studies by Halstead and others (1957). Models have been developed that display differing degrees of complexity and sophistication. The type of models range from those primarily concerned with the terrestrial surface and a shallow boundary layer above it (10 to 30 m), to those which are dynamic characterizations of the entire planetary boundary of the atmosphere and include the traditional Ekman spiral (surface to 1,000- or 1,500-m altitude).

Because there are a variety of models for use in surface energy budget studies, and because many of the workers in the field are less than completely familiar with numerical simulation of surface energy budget phenomena, this section first describes in general terms the model that has been used and then its application to the two-dimensional mapping of conditions that match the maps derived from remotely sensed data.

SURFACE ENERGY BUDGET MODELS

Models developed around the surface energy budget approach have been employed in a wide variety of applications that include agriculture (Halstead and others, 1957; Myrup, 1969), permafrost, and pack ice behavior (Outcalt, 1972a, b. and c). In general, the surface models can be subdivided into two groups: the first is based upon the dynamic equations of motion, with mass and energy related to wind and temperature in a series of discrete sublayers of the boundary layer; the second is based on the assumption of steady-state conditions with a constant downward longwave radiation from the atmosphere, lack of advective effects, and a clear or open sky. Both groups of models use data collected at a single point and therefore are spatially one-dimensional.

This study utilizes the second, the simpler steady-state model, but extends it spatially to two dimensions. Steady state was employed by Watson and others (1971) in a radiative-conductive surface model which, however, does not consider turbulent transfer of energy in the atmosphere, to describe geologic patterns according to differences in thermal characteristics of surface materials. Constant atmospheric inputs also have been used by Myrup (1969), Outcalt (1972a), Goddard (1974), and Kahle and others (1975).

THE OUTCALT CLEAR-SKY MODEL

Myrup (1969) pointed out possible applications of the energy-balance approach to the modeling of urban-rural temperature differences. Outcalt's (1971) digital version added several specific urban-oriented input parameters, which make the model both applicable to the study of the interactions of land use and land cover and climate and more easily extrapolated into a two-dimensional system which is based upon land use and land cover polygons. Because the current work is an exploratory inquiry, a clear-sky model which considered only low-velocity air movement was chosen to reduce the number of factors to be considered. The model is summarized in the following section.

The model is based upon the surface energy conservation equation (eq. 2), which can be rewritten as

$$R_n - H - LE - G = 0 \tag{24}$$

In this form, each of the four terms, or flux densities, are functions of an equilibrium, which is an inherent property of the surface energy balance for times that range from 1 second on up. If all other inputs to the model are known, either observed or derived, there will be only one surface temperature that will drive equation (24) to a zero equilibrium. Temperature is a controlling factor in each of the energy flows related to the four terms but is most obvious in the role it plays in R_n. An iterative algorithm is used to determine the one temperature that satisfies the equilibrium of the equation.

NET RADIATION

To expand the basic simulation model into a usable form, each of the flux densities of the energy flows must be examined separately. Flux densities are the intensities of energy flows and, for radiant energy, are values of R. Balance at the surface between downwelling radiation ($R\downarrow$) and upwelling radiation ($R\uparrow$) is separated into solar or shortwave (R_{sw}) and longwave (R_{lw}) components in the following equation:

$$R_n = (R_{sw}\downarrow - R_{sw}\uparrow) + (R_{lw}\downarrow - R_{lw}\uparrow). \quad (25)$$

Here, $R_{sw}\downarrow$ represents solar radiation incident upon the terrestrial surface and $R_{sw}\uparrow$ solar energy reflected by the surface. The difference in the pair of values is the solar radiation absorbed by the surface. Downwelling longwave radiation ($R_{lw}\downarrow$). is that emitted by the atmosphere, a small part of which (usually less than 10 percent) is reflected and is included with the surface emission in the term ($R_{lw}\uparrow$).

To calculate $R_{sw}\downarrow$ the following procedure is used. First, the solar beam received at any moment upon an imaginary plane parallel with the Earth's surface and at the outer edge of the atmosphere, per unit area is

$$Q_s = Q_{sc}\left(\frac{\bar{r}}{r}\right)^2 \cos Z \quad \text{and} \quad \frac{r_i}{\bar{r}} = r', \quad (26)$$

where Q_{sc} is the solar constant in W m^{-2}; $\bar{r}$ and r_i are the mean and instantaneous Earth-Sun distances, respectively; r' is the Earth-Sun distance when $\bar{r}=1$ and Z is the solar zenith angle. At any particular moment, Z is given by

$$Z = \cos^{-1}(\sin\phi\cdot\sin\delta + \cos\phi\cdot\cos\delta\cdot\cos h), \quad (27)$$

where ϕ is the latitude, δ is the solar declination (north positive), and h is the hour angle (morning negative).

Empirical expressions ascribed to Brooks by Gates (1962) are used to calculate the depletion of Q_{sc} by atmospheric scattering and, to a small extent, by absorption. If the sum of the Brooks expression is considered an extinction coefficient, combination with equation (26) yields:

$$Q = Q_{sc}\left(\frac{\bar{r}}{r'}\right)^2 \exp\left[-0.089\left(\frac{p\,m}{1013}\right)^{0.75} - 0.174 \quad (28)\right.$$
$$\left.\left(\frac{w_m}{20}\right)^{0.6} - 0.083\,(d\,m)^{0.9}\right]\cos Z,$$

where w_m is the precipitable water in the atmospheric column in millimeters, d is the dust and haze particle concentration in particles per cubic centimeter, and m is the optical air mass and is equal to sec $Z(p/1013)$.

In the case of a sloping surface, the term cos Z' replaces cos Z in equations 26 and 28 according to the relationship:

$$\cos Z' = \cos i\cdot\cos Z + \sin Z\cdot\sin i\cdot\cos(\alpha+\alpha'), \quad (29)$$

where i is the slope in degrees above the horizon, α is the solar azimuth angle and α' the aspect of the slope, both in degrees with respect to due south (east negative). The solar azimuth angle can be found from:

$$\alpha = \sin^{-1}(\cos\delta\cdot\sin h/\sin Z). \quad (30)$$

The complete expression for direct solar radiation at the surface is equation (28) with cos Z' substituted for cos Z.

In addition to the direct but attenuated solar beam, the total downwelling solar radiation reaching the surface includes diffuse radiation downscattered by air molecules and atmospheric aerosols. The diffuse radiation has two components. The larger is the solar radiation downscattered as part of the beam attenuation (q'), and the smaller is half of the scattering of surface reflected light (B). This back scattering is about 6 percent of the reflection because it is Rayleigh scattering. Mie scattering by aerosols is toward space and does not significantly add to the value of B. The combined term $(Q+q)$ is equivalent to $R_{sw}\downarrow$.

In the Outcalt model, the assumption is made that diffuse radiation received by the surface is equal to half that scattered by the atmosphere. This, of course, is a simplification that does not take into account the fact that most of the light scattered by particles as large as haze or dust reaches the surface as a part of the diffuse radiation because the light is forward scattered. The amount of forward scattering, however, depends upon the size distribution of the aerosol population and is therefore difficult to model without sophisticated input data. Lacking these data, the experimental inquiry in this paper used the simple assumption in the Outcalt model that all scattering is half upward and half downward. This assumption keeps the model intact but may underestimate the solar input slightly, especially if considerable atmospheric turbidity is also assumed. The calculation of diffuse downradiation is then:

$$q'=\left(\frac{Q_s}{2r'^2}\right)\cos Z\ \{1-\exp\ [-0.083\,(d\ m)^{0.9}]\}\ corr. \tag{31}$$

where *corr.* is a slope correction factor given by

$$corr.=\left[\ \cos\left(\frac{i}{2}\right)\right]^2. \tag{32}$$

B is treated as a separate term and is:

$$B\ =\ \frac{a}{2}\ (Q+q')\ 1-\exp\ -0.083\,(d\ m)^{0.9}\ corr. \tag{33}$$

The total downwelling solar radiation is, then,

$$R_{sw}\downarrow\ =Q+q'+B=Q+q, \tag{34}$$

and the net shortwave radiation at the surface is, therefore,

$$R_{sw}\downarrow\ -\ R_{sw}\uparrow\ =(1-a)\ (Q+q). \tag{35}$$

In most modern cities, multi-storied buildings create large areas of shadow. The downward solar flux is intercepted and only diffuse and backscattered radiation may reach the shadowed areas. The percentage of surface in shadow varies spatially, depending on the height and density of structures and vegetation, and also temporally, depending upon Sun angle. In Outcalt's urban model, calculations of the "shadow fraction" (SF) are based on an arbitrarily chosen function,

$$SF=(1-\cos Z)^3. \tag{36}$$

Accompanying the shadow effect, which causes a decrease in solar radiation at the surface, is the effect of the vertical faces of buildings that intercept the solar beam and increase the reflected load at the surface. Again, this reflected radiation component varies with Sun angle as well as with building configuration. To deal with this component, Outcalt (1971) considered the total solar radiation receipt for a vertical wall, rotated through the day so that the angle of its exposure at all times is equal to Z. The geometrical calculations involved here are identical to those for the surface. The total "upright" solar radiation receipt (R_{uprt}) is given by

$$R_{uprt}=Q_{uprt}+2q_{uprt}, \tag{37}$$

where Q_{uprt} is the beam radiation received by an illuminated wall and q_{uprt} the diffuse radiation received by a shadowed wall.

Combination of the additional "urban radiation" terms with the previously developed net solar radiation equation (35) produces

$$\begin{aligned}R_{sw}=\ &[(1-SF)\ (Q+q)\ +SF(q)\\&+R_{uprt}\ (S_1/S_2)]\ (1-a),\end{aligned} \tag{38}$$

where $q=q'+B$, S_1 is the silhouette area of the average building, and S_2 is the specific area or the average lot area of each building. The terms S_1 and S_2 are those defined by Lettau (1969) and will be used again in connection with the roughness length determination, the use for which he defined them.

Thermal radiation is calculated as a function of surface temperature and "effective sky temperature." The latter quantity is defined by Reifsnyder and Lull (1965) as the temperature "appropriate to" the total amount of longwave-emitted sky radiation; that is, the atmosphere is treated as a blackbody radiating at the effective sky temperature. Outcalt (1971) uses a constant daily effective sky temperature equal to the daily shelter-level mean temperature depressed by 22°C. The basic equation is then

$$R_{lw}=\epsilon\,(\sigma T^4_{sky}-\sigma\ T^4_o), \tag{39}$$

where R_{lw} is the longwave component of net radiation, T_{sky} is the mean temperature of atmospheric downradiation in °K, and ϵ is the emissivity of both surface and sky and is assumed to be unity. In an urban area, however, building walls are obstacles to downward longwave global radiation and the enhancement of ground radiation. Outcalt (1972b) takes the approach of Reifsnyder and Lull (1965, p. 34), who define the view factor for thermal radiation as "the fraction of the radiation leaving a surface in all directions that is intercepted by another surface." The view factor (F) is related to obstacle height (h_o) and the spacing of the obstacles (D) expressed by

$$F=\sin^2\left(\arctan\frac{D}{2h_o}\right). \tag{40}$$

Outcalt (1971) considers that the view factor (F') is equivalent to 2 times the silhouette ratio (S_1/S_2), previously defined:

$$F'=2\,(S_1/S_2). \tag{41}$$

Thus,

$$R_{lw}=\epsilon[\,(1-F')\,\sigma T^4_{sky}/\ (F-1)\,\sigma T^4_o]. \tag{42}$$

SENSIBLE HEAT AND LATENT ENERGY FLUXES

The fluxes of sensible heat and latent energy are represented by the traditional equations:

$$H=-\rho\ C_pK_h\frac{\partial\,\theta}{\partial\,z}, \tag{43}$$

and

$$LE=-\rho LK_w\frac{\partial\,q_w}{\partial\,z}, \tag{44}$$

where ρ is air density, C_p is air specific heat at constant pressure, L is the latent heat of vaporization, K_h and K_w are turbulent diffusivities for heat and water vapor, respectively, θ is potential temperature, q_w is specific humidity, and z is the height above the surface.

In the Myrup and Outcalt models the diffusivities for heat, water vapor, and momentum (K_m) are assumed to be equal. By utilizing the logarithmic wind relationship and solving for (K_m), K_h and K_w may also be found.

Under near neutral conditions, wind speed varies exponentially with height and may be expressed by the logarithmic wind profile equation (Sellers, 1965),

$$u = \frac{u^*}{k} : \ln \left| \frac{z}{z_0} \right|, \tag{45}$$

where u is the windspeed; u^* the friction velocity, k the Von Karman constant (0.04); and z_0 the roughness length, the height above the surface at which the wind speed is zero. Roughness length is calculated by the formula

$$z_0 = \frac{H\theta}{2} \cdot (S_1/S_2), \tag{46}$$

where $H\theta$ is the mean height of objects above the surface. Differentiating equation (45) with respect to windspeed and height gives

$$\frac{du}{dz} = \frac{u^*}{kz}. \tag{47}$$

The flux of momentum near the surface (r) is described by

$$r = \rho K_m \frac{\partial u}{\partial z}. \tag{48}$$

Substituting equation (48) in equation (47) gives

$$r = \rho K_m \frac{u^*}{kz}. \tag{49}$$

Thus,

$$K_m = \frac{rkz}{\rho u^*}, \tag{50}$$

and since, by definition,

$$u^* = (r/\rho)^{1/2}, \tag{51}$$

then

$$K_m = u^*\, kz. \tag{52}$$

The substitution of equation (51) for u^* yields

$$Km = \frac{k^2\, uz}{\ln|z/z_0|}. \tag{53}$$

Since it is assumed that $K_h = K_w = K_m$, the flux density equations become

$$H = \frac{-\rho C_P k^2\, u}{\ln|z/z_0|} \cdot \frac{\partial p_w}{\partial \ln|z|}, \tag{54}$$

and

$$LE = \frac{-\rho\, L\, k^2 u}{\ln|z/z_0|} \cdot \frac{\partial\, q_w}{\partial \ln|z|}, \tag{55}$$

To improve the model, Outcalt (1972b) added a stability correction term to equations (54) and (55) and obtained this sensible heat equation

$$H = \frac{-\rho C_P k^2 u}{\ln|z/z_0|} \cdot \frac{\partial q}{\partial \ln|z|} \cdot (|1 - 32\, Ri|)^{1/2} \tag{56}$$

where Ri is the bulk Richardson number according to Fleagle and Businger (1963, p. 193).

In finite difference form, equations 55 and 56 become

$$H = \frac{k^2 \rho\, C_P u}{[\ln|z/z_0|]^2} . (|1 - 32\, Ri|)^{1/2} \cdot (T_d - \Gamma z_d - T_0) \tag{57}$$

and

$$LE = \frac{-\rho L k^2\, u}{[\ln|z/z_0|]^2}\, (q_2 - q_0), \tag{58}$$

where Γ is the adiabatic lapse rate and T_d denotes the temperature at the atmospheric "damping" depth (z_d). Outcalt (1972b) defines this mixed-layer depth as that at which diurnal surface effects upon temperature and wind are almost completely damped out, that is, the depth of the mixed layer. Myrup uses 300 m as a constant damping depth for urban applications. Outcalt modifies this approach and calculates z_d as the level in the atmosphere at which two particular expressions for diffusivity converge.

These functions are

$$d_1 = \frac{k^2 u}{\ln|z_d/z_0|}, \tag{59}$$

a bulk diffusivity value, and

$$d_2 = \frac{z_d^2}{5.184 \text{ ex } 5}, \tag{60}$$

a thermal diffusivity term defined by Terzaghi (1952) as the damping depth for a 12-hour temperature wave in a homogeneous medium. In the iterative procedure used to find the convergent value of z_d, values of z_d are incremented in 1-cm steps from the roughness length, and the final value for z_d is obtained as the point at which the two functions converge. This admittedly simple approach results in values which vary spatially with surface roughness and from day to day depending on wind speed. The damping depth remains constant throughout the day, however.

SOIL HEAT FLUX

The soil heat flux G is described by the equation

$$G = k\frac{\partial(\rho C_s T_s)}{\partial z_s}, \qquad (61)$$

where k is the thermal soil diffusivity of the soil C_s represents the soil volumetric heat capacity (Sellers, 1965), T_s is the soil temperature and z_s is depth in the soil. The integrated form of equation (61) for the one-dimensional case is

$$G = -\rho\, C_s \frac{T_2 - T_1}{\int_{z_1}^{z_2} dz_s} \qquad (62)$$

where T_2 and T_1 denote soil temperature at depths z_2 and z_1, respectively. Diffusion here is considered to be purely a process of molecular conduction so that the thermal diffusivity can be considered independent of depth (Monteith, 1973).
Thus,

$$\int_{z_1}^{z_2} \frac{dz_s}{\kappa} = \frac{z_2 - z_1}{\kappa}. \qquad (63)$$

Substitution into equation (62) gives

$$G = -\rho\, C_s\, \kappa \frac{T_2 - T_1}{z_2 - z_1}, \qquad (64)$$

representing the soil heat flux term in a one-layer system. The Outcalt model treats a four-layer system using this same relationship, making possible the introduction of a realistic thermal lag into the diurnal soil temperature variations at different levels. The penetration depth of the diurnal temperature wave into the soil is calculated by the Terzaghi (1952) relationship used previously (eq. 61). The soil damping depth (z_G) is given by

$$z_G = (12t\kappa)^{1/2}, \qquad (65)$$

where $t = 4.32 \times 10^4$ sec (12 hrs).

The additional depths, $z_G/2$, $z_G/4$, and $z_G/8$ in the soil are used as nodes for the calculation of the soil heat flux term. At any particular level the rate and direction of temperature change is expressed by

$$\frac{dT_s}{dt} = \kappa \cdot \frac{\partial^2 T_s}{\partial z^2}. \qquad (66)$$

In finite difference form then, the temperature at depth z_2 in the soil at time increment I is given by

$$T_2(1) = T_2(I-1) + \kappa\frac{T_0(I-1) - 2T_2(I-1) + T_3(I-1)}{z_2^2}, \qquad (67)$$

where T_3 is the temperature at some depth $z_3 > z_2$.

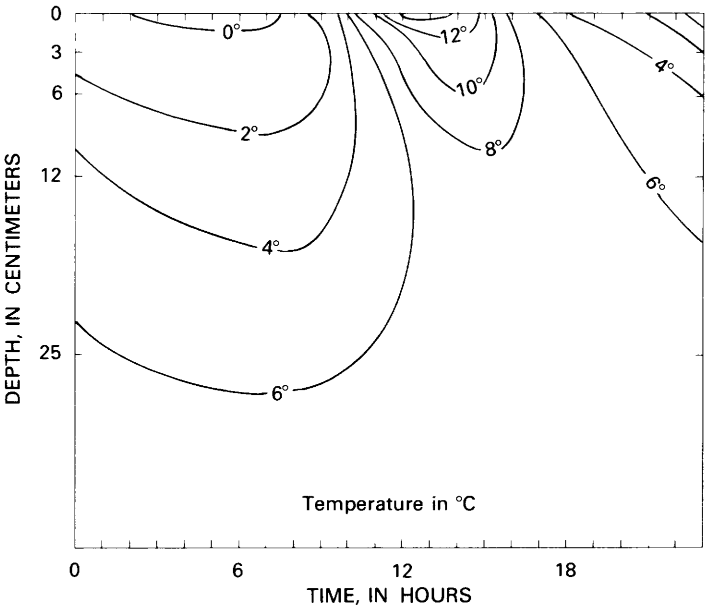

FIGURE 10.—Diurnal variation in substrate temperatures produced by the Outcalt clear-sky model.

The use of a set of similar equations, each corresponding to one of the five nodal depths, effectively introduces a lag in soil temperature change with depth. Figure 10 illustrates the nature of this lag for the case of a soil with thermal diffusivity of 0.005 $\text{cm}^2\ \text{sec}^{-1}$ for winter solstice, clear-sky conditions. Substrate thermal diffusivity is generally expressed in cgs units.

GENERAL FLOW OF THE MODEL CALCULATIONS

Input boundary conditions required for the Outcalt model were divided into three categories. These categories of inputs and their primary function in the simulation procedures are shown in table 6.

Computed boundary conditions include the penetration depths of both the atmospheric and substrate diurnal temperature waves (eqs. 60, 61, 65, and fig. 10), the atmospheric exchange coefficient (eq. 53), and the roughness length (eq. 46). The general flow of calculations is shown in figure 11.

TWO-DIMENSIONAL SIMULATION AND MAPPING

Land use and land cover information was coupled with a surface energy budget model in an attempt to predict the distribution of urban temperatures in

TABLE 6.—*Input boundary conditions for the Outcalt clear-sky model*

I. Temporal data	
Solar declination[1]	Radius vector of the Sun[1]
II. Meteorological data	
Atmospheric dust content[2]	Station pressure[2,8]
Air relative humidity[2,3,4,8]	Air temperature[4,8]
Precipitable water[2]	Wind velocity[4,8]
III. Surface characteristics	
Albedo[5]	Silhouette ratio[6]
Obstacle height[6]	Surface wet fraction[7]

[1] Required for the generation of diurnal values of solar radiation.
[2] Used in the calculation of the attenuation of the solar beam by atmospheric scattering and absorption.
[3] Used in the determination of the latent energy flux.
[4] Serves as boundary condition at the level of the atmospheric mixing height.
[5] Used in the calculation of solar radiation terms.
[6] Used in the calculation of the roughness length. The silhouette ratio is important in both solar and longwave radiation computations.
[7] Used in the calculation of specific humidity at the surface.
[8] At screen height.

Baltimore and its environs. Input parameters simulated the conditions that prevailed at the time of the imaging overpass of Skylab 3 at 10:05 a.m. EDT on August 5, 1973. With this timing, the map made from spacecraft-acquired data could be used to check the results of the simulation experiment. No attempt was made to simulate the budget of the entire imaged area, only of the smaller area shown in figure 1, in order to keep the simulation experiment within the limits of feasibility.

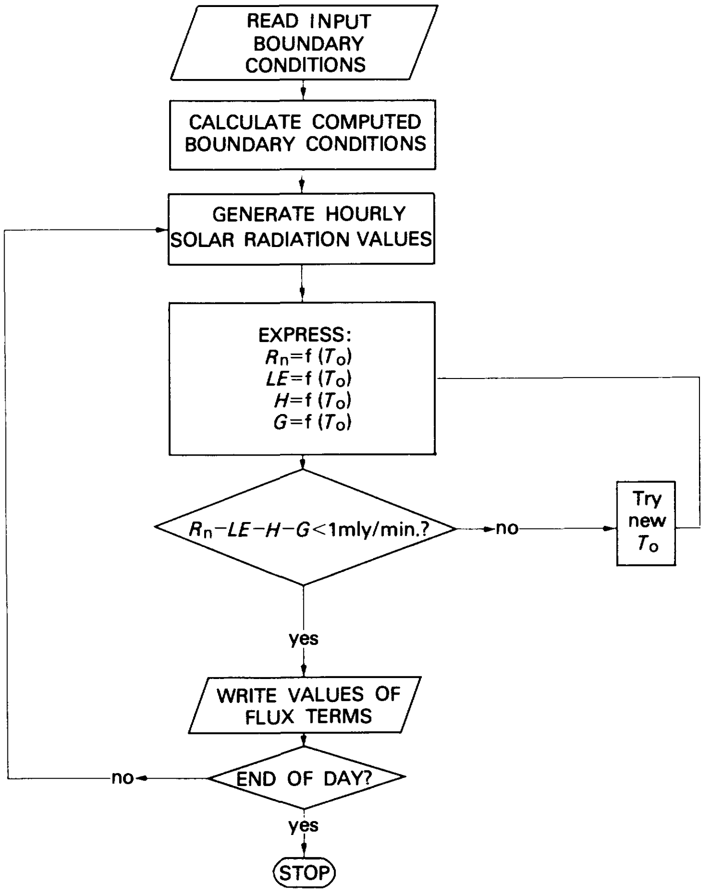

FIGURE 11.—Flow chart for the energy budget simulation model.

Land uses are superimposed on types of land cover. It is the interpretation of land use and land cover that supplies input values and sets input parameters for simulation. The degree to which this is true is indicated by comparison of the observed and the predicted patterns of radiation temperatures. From the historical standpoint, the relationship of land use and land cover to temperature was considered by Hammon and Duenckel (1902) and Duckworth and Sandberg (1954), who pointed out that the highest temperatures within a city were usually recorded at an urban core comprised of the CBD and industrial districts. Later, Chandler (1967) pointed out that the density and height of buildings, rather than their area, determined the effect of urbanization upon temperatures. Lewis and others (1971) conducted temperature traverses through Washington, D.C., and noted that temperatures were linked to land use and land cover. Subsequently, Nicholas (1974), in a detailed study, compared different land use and land cover classification schemes as indicators of surface roughness.

LAND USE AND LAND COVER CLASSIFICATION AND SOURCES OF INFORMATION

The choice of a land use and land cover classification system which can be used to effectively distinguish differences in surface characteristics that are significant in the creation of local climates is essential for accurate model input data. Frequently, land use classifications are based upon strictly economic appraisals. For example, distinction might be made between banking and retail sales activities, but not between high- and low-density residential uses. This type of classification does not provide suitable differentiation of surface characteristics for climatic simulation. Zoning classifications that include density specifications should be ideal for providing data on pavement fraction and building spacing, but they often indicate only potential use and may not represent the actual land cover conditions of urban surfaces at a given time. Finally, the classification scheme selected must provide information for all parts of an urban area, not just the city center; and the scheme should be applicable to other urban areas as well.

To facilitate State and national land use planning, the U.S. Geological Survey developed a land use and land cover classification system for use with remotely sensed data (Anderson and others, 1972 and 1976). This classification is particularly well suited for specifying surface characteristics that can be used as simulation inputs because land cover is included together with land use designations. A modification of the original Anderson system has been used for the energy budget mapping by numerical simulation described in this study. The classification is hierarchical, with two levels specified (table 7). The authors of this system realized that no single system of land use and land cover classification is suitable for the needs of all potential users and suggested that further breakdowns into third and fourth levels be developed by the user. Nicholas (1974) has suggested a third level suitable for the purposes of urban climate simulation.

TABLE 7.—*Land use and land cover classification system for use with remotely sensed data*

[Level I classification in boldface type; Level II in lightface]

1. **Urban and Built-up Land**
   01. Residential
   02. Commercial and Services
   03. Industrial
   04. Extractive
   05. Transportation, Communications, and Utilities
   06. Institutional
   07. Strip and Cluster Settlement
   08. Mixed
   09. Open and Other
2. **Agricultural Land**
   01. Cropland and Pasture
   02. Orchards, Groves, Bush Fruits, Vineyards, and Horticultural Areas
   03. Feeding Operations
   04. Other
3. **Rangeland**
   01. Grass
   02. Savannas (Palmetto Prairies)
   03. Chaparral
   04. Desert Shrub
4. **Forest Land**
   01. Deciduous
   02. Evergreen (Coniferous and Other)
   03. Mixed
5. **Water**
   01. Streams and Waterways
   02. Lakes
   03. Reservoirs
   04. Bays and Estuaries
   05. Other
6. **Nonforested Wetland**
   01. Vegetated
   02. Bare
7. **Barren Land**
   01. Salt Flats
   02. Beaches
   03. Sand other than Beaches
   04. Bare Exposed Rock
   05. Other
8. **Tundra**
   01. Tundra
9. **Permanent Snow and Icefields**
   01. Permanent Snow and Icefields

Source: Anderson and others, 1972.

LAND USE AND LAND COVER DATA COLLECTION

A land use and land cover map that employs the two-level classification of table 7 is available at a scale of 1:100,000 for the Baltimore metropolitan area (U.S. Geological Survey, 1973). The photomosaic base for the map is gridded in square-kilometer cells of the Universal Transverse Mercator grid system. The portion of the map that includes the simulation site is shown at a reduced scale in figure 12.

The sizes of land use and land cover polygons vary considerably; the smallest mapped units are about $0.04\ \text{km}^2$. Ideally, the area of each polygon within a given sampling cell $(1\ \text{km}^2)$ should be accurately measured with a planimeter, or tabulations from digitized maps should be used to obtain the exact percentages of each land use and land cover type. Each of these methods, however, requires many man-hours of effort. As an alternative, a sampling scheme to collect and aggregate land use and land cover information from the map was employed in this study.

Urban climates can be examined at a variety of scales. Interest can focus on a single urban "thermal canyon," or the city can be viewed as a unit made up of a mosaic of Level II or more detailed uses. A knowledge of the dimensions of individual buildings that make up a street corridor in the CBD and the reflectivity of each building surface is necessary to model the radiation climate at a microscale. A mesoscale analysis may be based upon typical microstudies but also may be based upon analyses of general conditions that prevail in each land use and land cover type. A good example of the latter approach is to be found in the work of Nicholas (1974).

The present simulation study is on a mesoscale and covers, therefore, a rather large area. Treatment of block-by-block variations in input parameters to the model is not feasible. Furthermore, land use and land cover maps are not available for a microscale examination. Following procedures outlined by Jenner (1975), an aligned sample of eight points was taken to create an average value for a square-kilometer sampling cell. The values of the land use and land cover types upon which each of the points fell were averaged to obtain the value for the entire map data cell. The disadvantages frequently associated with this approach (Berry and Baker, 1968) do not apply here because the scale used is too coarse

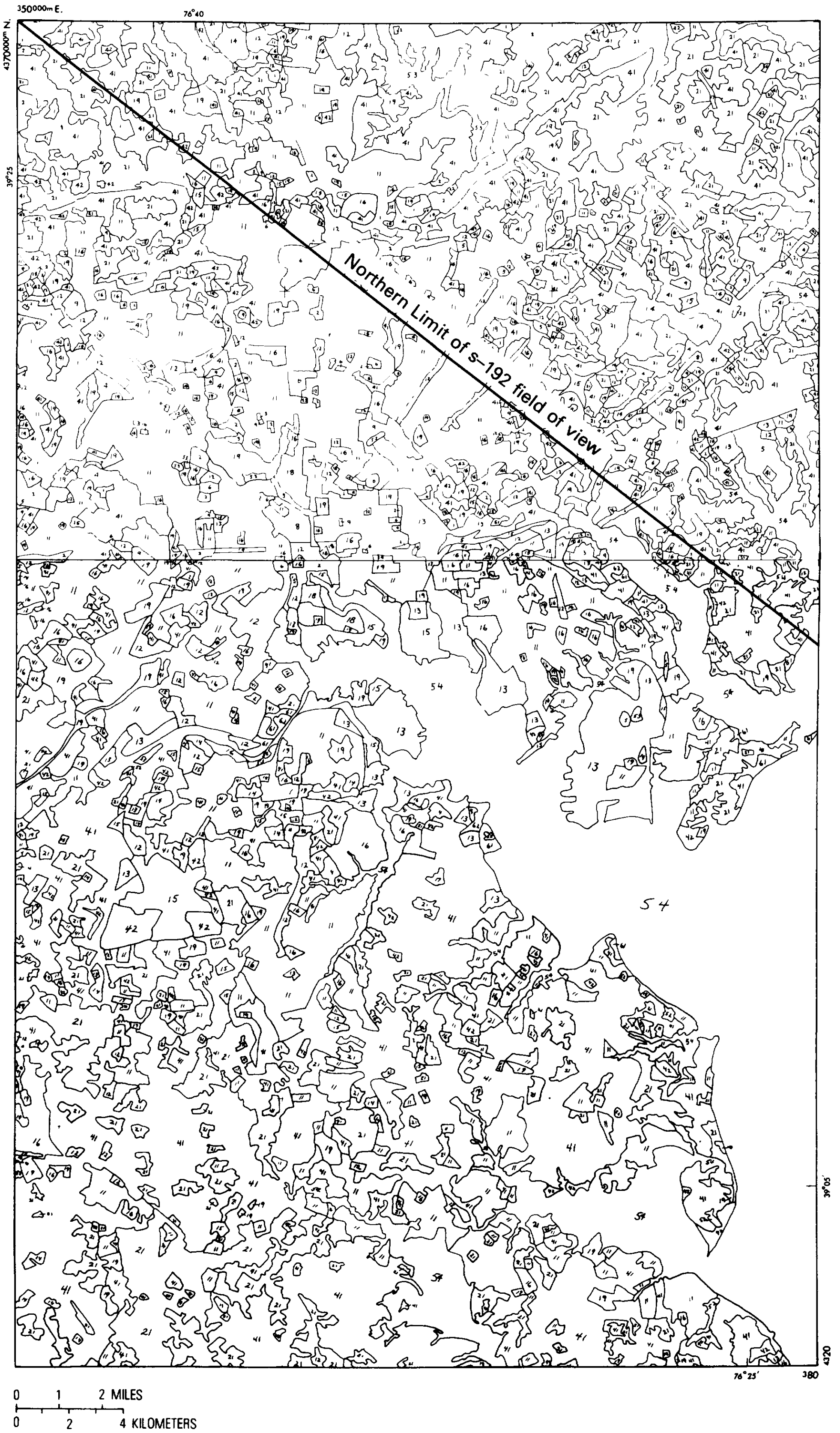

FIGURE 12.—Land use and land cover in the Baltimore area. Category designations appear in table 7 (U.S. Geological Survey, 1973).

to pick up block-by-block periodicities in land use and land cover characteristics.

Land use and land cover information was extracted directly from the CARETS land use and land cover maps of the U.S. Geological Survey (1973). Adjustments were made in the classification system to more greatly differentiate characteristics useful in the simulation. With the aid of high-altitude aerial photographs, a subdivision was made between high- and low-density residential use, and "institutional lands" (schools and hospitals, for example) were treated as a combination of commercial and open land. Completely open lands were modeled as parks, and "strip " and mixed uses were classed as commercial.

SURFACE CHARACTERISTICS ASSOCIATED WITH LAND USE AND LAND COVER TYPES

The energy balance simulation model requires the following input data related to surface characteristics: (1) roughness length, (2) silhouette ratio, (3) wet fraction, (4) substrate thermal diffusivity and heat capacity, (5) surface albedo, and (6) surface emissivity. These terms are discussed in the following paragraphs.

For Baltimore, Nicholas (1974) calculated typical values for roughness length by the Lettau (1969) formula and developed a third level for the U.S. Geological Survey land use classification system based upon variations in z_0. In the present study, the values of z_0 assigned to specific land use and land cover types are based upon the Nicholas results, as are typical silhouette ratios (table 8).

Values of the surface wet fraction (*WF*) were determined from high-altitude aerial color-infrared photographs. Because the WF at this season was closely related to the extent of vegetated areas, its value was readily determined from red plant signatures on the photographs. Association of these values with land use and land cover is also included in table 8.

For the simulation, soil heat capacity was held at a constant 0.5 calories cm^{-3} $°\text{C}^{-1}$. Typical thermal diffusivity (K) values for soil and artificial surface, are 0.005 $\text{cm}^2\ \text{sec}^{-1}$ and 0.020 $\text{cm}^2\ \text{sec}^{-1}$, respectively. Values of (K) associated with land use types were made a function of WF by the relationship:

$$K = [0.005WF + 0.020(1 - WF)]. \qquad (68)$$

Variations in albedo over a city are caused by both the diversity of surface materials and by building geometry, together with the effects of multiple reflections. Albedos of urban surfaces, determined from aerial studies, generally range from 0.11 to 0.25 (table 8).

TABLE 8.—*Values of surface characteristics used as inputs for each land use and land cover category in the simulation model*[1]

Category	a (percent)[2]	z_0 (cm)	WF (percent)	S_1/S_2 (ratio)[3]
Residential:				
High-density	14	151	5	0.19
Low-density	18	73	60	0.13
Commercial and services	15	78	5	0.02
Industrial	15	90	10	0.10
Extractive	12	3	10	0.01
Transportation	15	6	15	0.02
Open	22	80	90	0.71
Cropland	20	25	95	0.01
Orchard	20	115	90	0.25
Forest:				
Heavy[4]	22	127	95	0.25
Light[5]	22	25	90	0.25
Nonforested wetland	18	10	95	0.25
Beaches	10	2	15	0.00

[1] Data from Nicholas, 1974.

[2] Data from Kung and others, 1964; Barry and Chambers, 1966; Pease and Nichols, 1976.

[3] Derived from equation (38).

[4] Designates 40 percent or more crown density.

[5] Designates 10 to 40 percent crown density.

The ϵ value of 0.90 applied to all surfaces was based upon values cited by Sellers (1965) for almost all natural and manmade surfaces. In the simulation, the value applies to the whole spectrum of the thermal infrared and therefore does not contradict the value of 0.95 used in the remote mapping experiment for the scanner sensing bands. Between wavelengths of 8 μm and 13 μm, virtually all values of ϵ are greater than 0.90 (Wolfe, 1965, p. 75).

SIMULATION OF SURFACE TEMPERATURE DISTRIBUTION

The approach for modeling the spatial distribution of surface temperatures follows that developed by Jenner (1975). For each land use and land cover type, a set of surface characteristics is input into the model, along with prevailing synoptic weather parameters. The output includes the surface radiant temperatures associated with that land use and land cover type. The average surface temperature for a single square kilometer grid cell is given by

$$T_{i,j} = \left(\sum_{k=1}^{m} f_{i'j'k} \cdot T_k \right) / n, \qquad (69)$$

where k denotes the land use and land cover type and a total of m land use and land cover types is considered; T_k is the simulated temperature associated with land use and land cover type k; $f_{i,j,k}$ is the frequency of land use and land cover type k

TABLE 9.—*Meteorological conditions over Baltimore, Md., 10:05 a.m. EDT, August 5, 1973*

[Source: National Weather Service]

Meteorological parameter	Value
Station pressure	1015.0 mb
Precipitable water	40 mm
Dust content	[1] 3 particles cm^{-3}
Mean air temperature	24.0°C
Mean air relative humidity	61 percent
Mean wind velocity	270 cm sec^{-1}

[1] According to the Brooks solar generator model as restated by Gates (1962). The value should be considered only a relative indicator of turbidity and has no real relationship to the actual aerosol population.

within the cell i, j; and n is equal to the number of sample points in the grid cell.

The rationale is that each land use and land cover type contains a mix of surface properties that contribute to a characteristic temperature regime. The average temperature of a grid cell was the spatial average of the temperatures of 8 sample points representing different land use and land cover types.

Meteorological data for the Baltimore area, at 10:05 a.m. EDT, on August 5, 1973, are listed in table 9. Surface temperatures associated with specific land uses and land covers are listed in table 10, as generated for 10:05 EDT of the test day. The spatially averaged temperature distribution for the entire simulated area is mapped in figure 13.

A COMPARISON OF SIMULATED AND OBSERVED SURFACE TEMPERATURE PATTERNS

Both the map made by simulation (fig. 13) and the map made from remotely sensed data (fig. 14) show the general heat island structure of the city of Baltimore and the satellite heat islands of outlying commercial centers. Patterns of temperature distribution on the two maps have a general similarity but differ with respect to ground resolution and specific temperature values.

TABLE 10.—*Simulated surface temperatures of each land use and land cover type, Baltimore area, 10:05 a.m. EDT, August 5, 1973*

Land use and land cover type	T°C
Residential:	
High-density	30.9
Low-density	24.9
Commercial	30.8
Industrial	30.1
Extractive	35.0
Transportation and Utilities	36.9
Institutional	27.2
Strip	30.8
Mixed	30.8
Open	25.4
Cropland	24.2
Orchard	22.7
Forest by crown density:	
Heavy (40 percent or more)	22.3
Light (10 to 40 percent)	26.6
Water	24.0
Nonforested Wetlands	26.3
Beaches and Sand	34.9

Patterns on the map made from spacecraft-acquired information, the "observed" map, are more intricate than those shown on the map of the simulated temperature field. This difference indicates a greater spatial smoothing of data in the simulation process, where the 1-km^2 cell was nearly four times as large as the 0.52-km^2 cell used in making the observed map. The difference in resolution also arises from the fact that the simulation data cell included an average of only eight points taken from random-sized land use and land cover polygons, while the smaller remotely observed cell included an average of 100 pixel values derived from a more comprehensive surface analysis.

There is a noticeable difference between the two maps in the orientation of the axis of the Baltimore heat island: the horizontal axis of the observed map has a more northwesterly trend than the east-west axis of the simulation map. This discrepancy points out the need for Level III land use and land cover mapping. The northernmost city boundary, an east-west line, was used to separate high- and low-density residential areas in the simulation because of the lack of a mapped boundary between these two residential types on the land use and land cover map.

A comparison of radiation temperatures of specific target areas on the simulated-data and observed-data maps indicates that simulated values are conservative. This is most obvious in the Baltimore CBD, where temperatures are highest, and the discrepancy is on the order of 6° to 8°C. On the simulated-data map, these temperatures fall in a hierarchical interval of 34° to 37°C, whereas on the observed-data map they slightly exceed 41°C. Jenner (1975) found similar discrepancies when she applied the same modeling approach to Washington, D.C., and its environs and further ascertained that daily maximum temperatures were most prone to to this error. Possible causes for the discrepancy are given below.

APPRAISAL

The completion of this inquiry has indicated avenues for improvement and further study. Appraisal of results and suggestions for improvements and further investigation are discussed in the following sections.

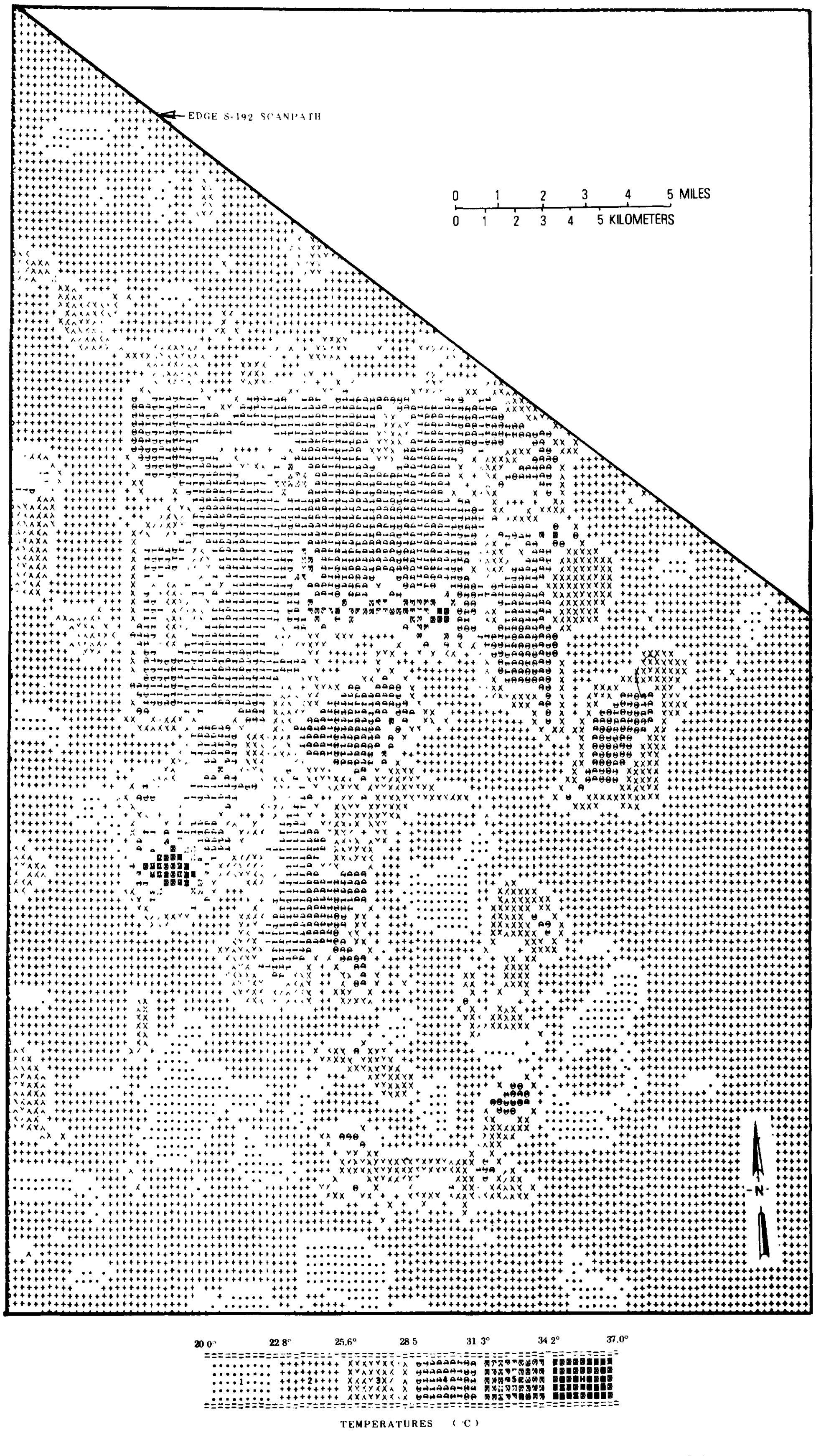

FIGURE 13.—Simulated surface radiation temperatures in the Baltimore area, 10:05 a.m. EDT, August 5, 1973.

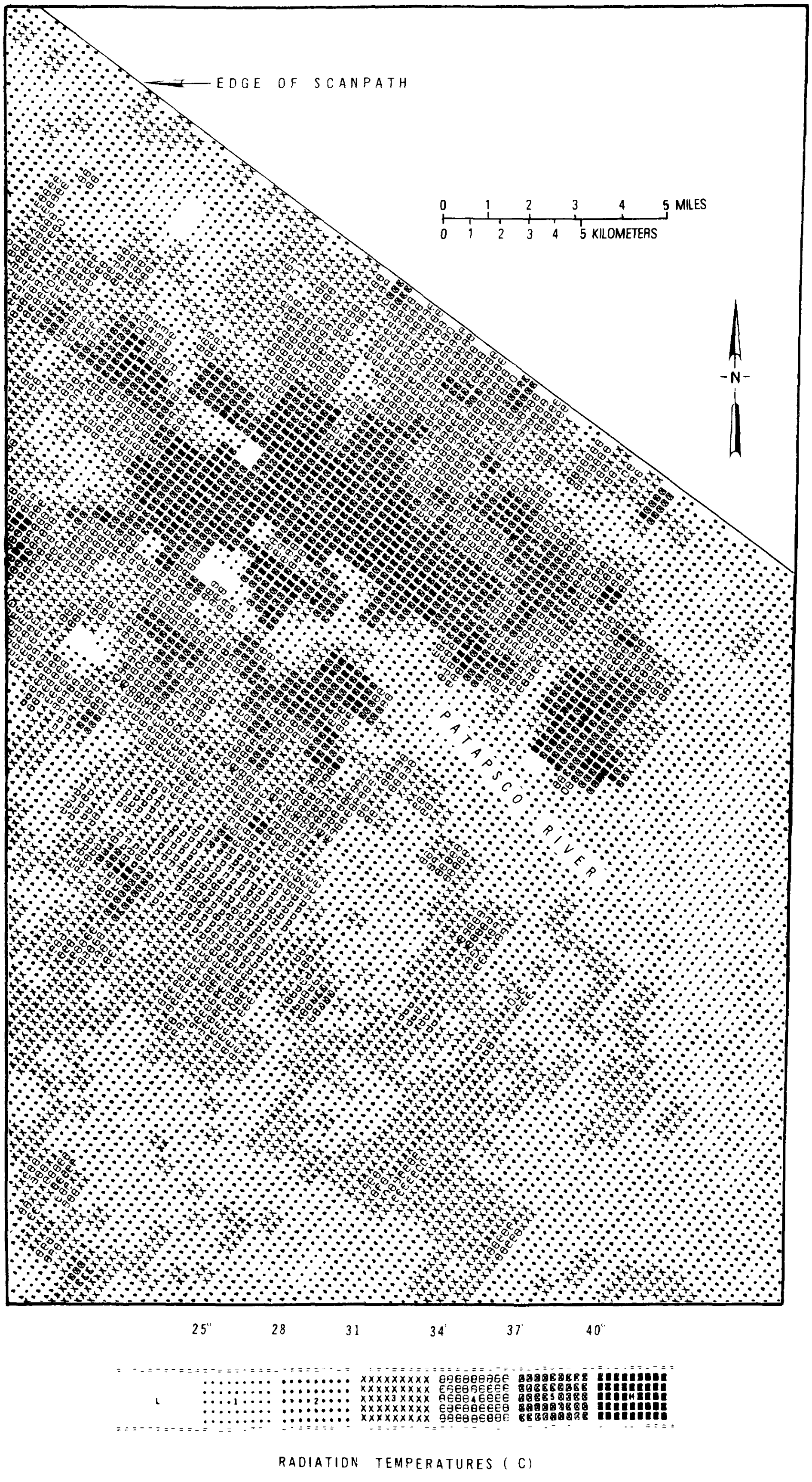

FIGURE 14.—Observed surface radiaion temperatures, in degrees Celsius, in the Baltimore study area, constructed as a line-printed graymap for comparison with the map of simulated temperatures. Remotely sensed information is from the Skylab S-192 multispectral scanner, band 13, scientific data output channel 21.

ENERGY BALANCE MAPS FROM REMOTELY SENSED IMAGERY

An understanding of the relationships between turbid air transmissivity in the visual wavelengths and the corresponding transmissivity in the thermal infrared is based upon the theoretical calculations of McClatchey and others (1972) at the Air Force Cambridge Research Laboratories. Experimental verification of this theory is still tenuous and is handicapped by the existence of gaseous pollution absorption and emission bands in the scanner sensing windows. Inquiry into the effects of gaseous pollution is still in an embryonic state, as the study of analogous conditions at San Bernardino indicates (see section on "Calibration Using Characteristics of the Atmosphere"). The nature of the scattering of radiation with wavelengths near 10 μm by aerosols makes necessary a correction factor for remotely sensed absolute radiation values, which in turn necessitates the use of at least one calibration target. Because of this necessity, the study could meet the goal of no calibration target only with a possible 5-percent error.

This is a phase of atmospheric optics that needs more study. With present knowledge, perhaps the "safest" values of downward atmospheric radiation would be those measured with a broadband longwave radiometer on the ground at the time of the scanning overpass.

Although the primary effort of this inquiry has been to map surface radiation temperatures derived from the thermal-infrared spectral sensing band of the S-192 multispectral scanner, a lesser effort has been expended to develop ways to map surface albedos from shortwave sensing channels and to map the distribution of surface net radiation from the combination of data from thermal and shortwave channels. The use of a single channel to sample albedos is a shortcut. Results appear rational despite the narrow spectral window used (0.68–0.75 μm) because the band straddles the sharp peak in chlorophyll absorption. Significantly prominent absorption bands outside of the sampling band, however, can cause errors of some magnitude. A case in point is the albedo of snow, which is too high because the water absorption band at 1.4 μm is not measured (Dirmhirn, 1968). Broadening the sample by using two channels, one on either side of the peak in chlorophyll reflectance, should give consistently better results.

A test of the accuracy of albedo mapping is an evaluation of the accuracy of derived values of net radiation, because these values combine information from the albedo sampling band with that from the thermal-infrared band. Any great error in ascertaining surface albedos would result in irrational net radiation values. The values of surface net radiation appear reasonable, however, considering the warm and humid surface boundary layer of the atmosphere that prevailed during the test. A net radiation value of 732 Wm^{-2} for the water surface of Chesapeake Bay may seem a little low, but the low value may be due to the slowing of the evaporation process by humid air.

The maps of the surface energy budget phenomena show the energy balance effects of different land use and land cover types and add to our understanding of the impact on climate of the diversity of manmade and natural surface elements. The fact, the shape, and the intensity of the urban heat islands in midsummer are shown. Forested lands, together with Chesapeake Bay, form cool annuli around the urban areas. These annuli conceivably could resist the movement of air in the lower boundary layer toward the cores of the cities. It is of interest to note that wooded lands have radiation temperatures similar to that of the air over the water surface of Chesapeake Bay. This may well reflect the fact that leaf temperatures are similar to that of the air that surrounds them, and the air temperature in the lower boundary layer is closely related to that of Chesapeake Bay under conditions of regional air stagnation.

Although the absorption of solar energy by city cores is relatively high, it is apparently offset by the high surface energy emission that is responsible for the heat island effect. Net radiation, the absorption of radiative energy into the terrestrial substrate system, is about the same as for surrounding nonurban lands. The maps demonstrate, then, that cities are not islands of high intake of radiative energy despite their existence as islands with temperatures higher than the surrounding environs.

Clouds comprise unwanted mapping noise. A cloud appears on the maps as a spot of comparatively low radiation temperature, high albedo, and slightly low net radiation when the temperature and albedo anomalies are combined. Cloud shadows are spots of slightly low temperature and false low albedo, a combination that produces areas of false high net radiation when compared with surrounding areas with the same land use and land cover. When the percentage of cloud cover is more than minimal, mapping by remotely sensed data becomes impossible. Cloudiness is a constraint upon the utility of the remote information gathering procedure.

These are but a few observations and applications of the information that can be gleaned from synoptic maps of surface energy balance phenomena made from remotely gathered data. Substantial success has been achieved in using multispectral scanners as imaging radiometers to acquire the necessary data and construct these maps, but the problems mentioned in the appraisal still need to be investigated and, with knowledge so gained, the methods improved.

ENERGY BUDGET SIMULATION

The noteworthy achievement of the simulation mapping experiment has been the development of ways to extend the Outcalt simulation model into a spatially two-dimensional form suitable for the construction of maps. Temperature distribution patterns so derived agree in form with those on maps made from multispectral scanner data but have poorer resolution of pattern features. Temperature ranges and hierarchies are similar to those on maps of remotely sensed data, but absolute temperatures are lower. There is the possibility, of course, that either or both of the mapping methods are in error, but the remotely sensed map data correlate better with ground-measured values. The following is an examination of possible sources of error in the simulation.

The conservative nature of the model, as regards temperature, may have several possible causes. In equation (31), half of the diffuse solar radiation is assumed to be scattered toward space, whereas, in reality, this probably does not occur. Only Rayleigh-scattered radiation fits this specification, and its value amounts to less than 6 percent of the solar constant. Pure Rayleigh scatter is seldom experienced at the surface; more commonly it is a mixture of diffuse radiation produced both by air molecules and much larger aerosols. Since scattering by aerosols is predominantly forward, only a small amount of solar radiation is lost to the surface by atmospheric turbidity. Pyranometric readings on smoggy days are almost as high as on clear, nonturbid days, perhaps being deficient by only a few percent. If half of the solar radiation is scattered by aerosols back into space, the value of solar input to the surface is reduced and simulated temperatures may be lower-than-real. A restructuring of equation (31) would result in a more realistic solar generator for the model.

Another need in the model is a valid statement of turbidity (eq. 28). In the Outcalt model, dust and haze concentrations of one to three particles per cm^3 have been used. The definition in equation (28) of the dust and haze particle concentration as particles per cubic centimeter is meaningless because the definition does not specify the size distribution of the aerosol population. According to McClatchey and others (1972), small haze particles, with radii of 0.10 μm, average about 19,000 per cm^3 in the first 10 km of the atmosphere when the meteorological visibility is 5 km at the surface. Under the same conditions of visibility, particles with radii of 1.0 μm average only 1.5 per cm^3. A definition that approximates values used in the current form of the solar generator model is the number of counts per cubic centimeter of particles with radii of 1.0 μm, averaged over the first 4 km of an atmospheric column as follows: five samples in all, with counts taken at the surface and 1-, 2-, 3-, and 4-km levels. The definition of symbol (d) in equation (28) is changed from that of a dust and haze particle concentration to a "dust factor," on the basis of the above description. A graph which relates that dust factor to meteorological visibility is shown in figure 15. The graph is based on the assumption of a typical distribution of aerosols upward from the surface and may need modification if a pronounced inversion traps particulates.

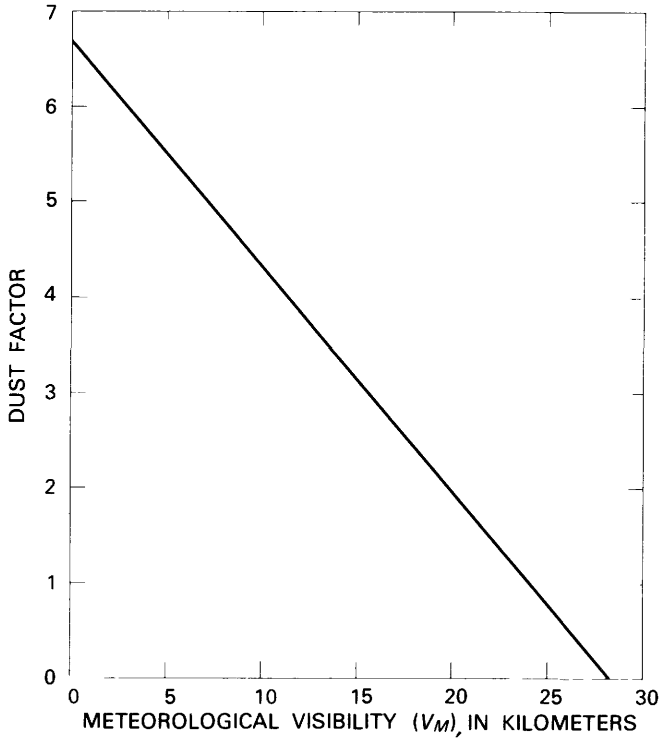

FIGURE 15.—The dust factor as a function of meteorological visibility. (Data from McClatchey and others, 1972, p. 8–9).

Other possible causes for the conservative nature of the model are the assumption of a constant diurnal damping depth, the assumption that the longwave radiant temperature of the sky is a constant 22°C below the sensible air temperature at screen height, and the use of general constants for soil heat flux diffusivity and heat capacity.

In addition to needed refinements of the model, attention should be focused upon a land use and land cover classification with more detail relevant to surface energy balances and related temperatures. Land use and land cover classes, as mapped, generalize small terrain features such as houses, lawns, and fields, and small areas of forest. This generalization was particularly bothersome in the current study because no demarcation was provided between high- and low-density residential areas, whereas the two have markedly different energy balance characteristics. This suggests that a third level should be devised with classification definitions not only applicable to a wide variety of sites but pertinent to energy transformations. In brief, within basic land use and land cover categories, there should be more detailed sampling of the heterogeneous features now classified within a single use.

Further inquiry should be carried out regarding methods for obtaining average values of simulation sampling cells. Perhaps actual area averages obtained by automated means might well be better than the eight-point sampling approach used in the current study. Much might be learned from a comparison of the simulated-data and observed-data maps by using such statistical analyses as two-dimensional spectral analysis (Rayner, 1971).

THE COUPLED EXPERIMENT

The coupling of the experiments has tested the two approaches for making synoptic maps of surface energy exchange phenomena against each other. This method of testing has been expedient for the current experiment, but the question may well be asked regarding the utility of doing so in the future.

Mapping with remotely sensed data permits maps to be constructed both of moderately large areas and with good resolution. Maps made with 20-pixel averaging cells have a resolution quite comparable to land use and land cover polygons in the Washington-Baltimore area. The degree of averaging is sufficient to reduce the noise created by anomalous pixel values and give a degree of consistency that makes comparison with land use and land cover polygons valuable. Relation between energy exchange and land use and land cover patterns can be readily observed, but there is no insight into causes of existing relationships without analysis of the effect of inputs into numerical simulations of the patterns. The observed-data maps show land use and land cover/energy budget relations, whereas the numerical simulation shows the causes of the relations.

The maps made in this study are for close-to-an-instant of time. But we know that no energy balance relations are static. Constantly changing energy transfer balances react to diurnal and seasonal changes. Increasing turbidity or cloudiness also alters inputs to these intricate surface energy transformation systems. Continual changes can be recorded on a series of maps, but there are at present severe restrictions on gathering sufficient data to do so. Periodic changes can be simulated, however, and, because numerical models are closely tied to land surface parameters, the changes can be simulated. In so doing, the ways that changing surface inputs affect the energy balances can be ascertained.

The coupling of the techniques in the current inquiry is intended to give insight into the potential utility of mating the remote acquisition of energy balance data with numerical simulation.

SUMMARY

The purposes of this study have been threefold: (1) the development of techniques for mapping the surface distributions of basic energy balance phenomena from an orbiting spacecraft, (2) the development of techniques for mapping surface radiation temperatures by numerical simulations, and (3) the combination of the two techniques to achieve an incisive understanding of the relations of man's use of the land to local and regional climates. Both 1 and 2 are valid lines of inquiry in their own rights but find common ground in the energy conservation equation (eq. 2).

Each of the terms of the equation—net radiation, soil heat flux, the sensible heat flux across the surface-to-air interface, and the heat energy that becomes latent when water evaporates or a plant transpires—is a complex function of a set of variables. A number of these variables can be assessed by remote sensing methods. The wet fraction of soil, as represented by vegetation cover, and surface features that produce aerodynamic roughness are amenable to traditional photointerpretation.

Several of the variables, however, require fairly sophisticated measurement, difficult to achieve on a two-dimensional surface. For this reason, an electro-optical scanner was used as an imaging radiometer to map the surface distributions of radiation temperatures, albedos, and net radiation.

The energy conservation equation is the common base that permits remotely observed measurements of energy balance phenomena to provide both inputs for the simulation model and as checks as to its accuracy. The current study, however, has been more concerned with the development of the two sets of techniques than in the use of one technique to gather information for the other.

The surface characteristic chosen for comparison of the two techniques, or approaches, is the thermal state expressed by the distribution of radiation temperatures. Using the approaches described in the current study, however, it is possible to run similar experiments with other data sets by changing land use and land cover parameters to match both urban and rural land uses and land covers and their climatic impact.

The use of a numerical simulation model in conjunction with analyses of maps derived from multispectral scanner data is a promising approach to the study of land use climatology. Measurements can be made by the scanner that are difficult to impossible to make from the ground, and these measurements can be augmented by simulation. It is entirely possible that, by reversing the research approach, a more useful land use and land cover classification, suitable to a new subdiscipline, can be devised using a satellite multispectral scanner system. Such inquiries will be aided by research agencies that are aware of the benefits of understanding man's impact on climate.

REFERENCES

Alexander, R. H., Lewis, J. E., Lins, H. F., Jenner, C. B., Outcalt, S. I., and Pease, R. W., 1976, Applications of Skylab data to land use and climatological analysis: National Aeronautics and Space Administration, Type III Final Report under Skylab/EREP Investigation No. 469, Pt. A (CARETS), NTIS E77-10123.

Anderson, J. R., Hardy, E. E., and Roach, J. T., 1972, A land-use classification system for use with remote-sensor data: U.S. Geological Survey Circular 671, 16 p.

Anderson, J. R., Hardy, E. E., Roach, J. T., and Witmer, R. E., 1976, A land use and land cover classification system for use with remote sensor data: U.S. Geological Survey Professional Paper 964, 28 p.

Barry, R. G., and Chambers, R. E., 1966, A preliminary map of summer albedo over England and Wales: Quarterly Journal of Royal Meteorological Society, v. 92, p. 543–548.

Berry, B. J. L., and Baker, A. M., 1968, Geographic sampling, *in* Berry, B. J. L., and Marble, D. F., eds., Spatial Analysis: Englewood Cliffs, N. J., Prentice-Hall, p. 91–100.

Chandler, T. J., 1967, Night-time temperatures in relation to Leicester's urban form: Meteorology Magazine, v. 96, p. 244–250.

Dirmhirn, Inge, 1968, On the use of silicon cells in meteorological radiation studies: Journal of Applied Meteorology, v. 7, no. 4, p. 702–707.

Duckworth, F. S., and Sandberg, J. S., 1954, The effects of cities upon horizontal and vertical temperature gradients: Bulletin of American Meteorology Society, v. 35, p. 198–207.

Fleagle, R. G., and Businger, J. A., 1963, An introduction to atmospheric physics: New York, Academic Press, 346 p.

Gates, D. M., 1962, Energy exchange in the biosphere: New York, Harper and Row Biological Monographs, 151 p.

Goddard, W. B., 1974, A climate simulation model applied to arctic pack ice: Aidjex Bulletin, no. 25, p. 55–73.

Halstead, M. H., Richman, R. L., and Merryman, J. D., 1957, A preliminary report on the design of a computer for micrometeorology: Journal of Meteorology, v. 14, no. 4, p. 308–325.

Hammon, W. H., and Duenckel, F. W., 1902, Abstract of a comparison of the minimum temperatures recorded at the U.S. Weather Bureau and the Forest Park Meteorological Observatories, St. Louis, Mo., for the year 1891: Monthly Weather Review, v. 30, no. 1, p. 12–13.

Hudson, R. D., 1969, Infrared system engineering: New York, John Wiley, 642 p.

Jenner, C. B., 1975, Simulation of land-use effects on the urban temperature field: Unpublished Ph.D. dissertation on microfilm at the University of Maryland, College Park.

Junge, C., 1963, Atmospheric chemistry and radioactivity: New York, Academic Press.

Kahle, A. B., Gillespie, A. R., Goetz, A. F. H., and Addington, J. D., 1975 Thermal inertial mapping: 10th International Symposium on Remote Sensing of Environment, Ann Arbor, Michigan, 1975, Proceedings, p. 985–994.

Kondratyev. K. Ya., 1969, Radiation in the atmosphere: New York, Academic Press, 912 p.

Kung, E. C., Bryson, R. A., and Lenschow, D. H., 1964, Study of a continental surface albedo on the basis of flight measurements and structure of the Earth's surface cover over North America: Monthly Weather Review, v. 92, no. 12, p. 543–564.

Lettau, H. H., 1969, Note on aerodynamic roughness parameter estimation on the basis of roughness element description: Journal of Applied Meteorology, v. 8, no. 5, p. 828–832.

Lewis, J. E., Nicholas, F. W., Scales, S. M., and Woolum, C. A., 1971, Some effects of urban morphology on street-level temperatures at Washington, D.C.: Washington Academy Sciences Journal, v. 61, p. 258–265.

McClatchey, R. A., Fenn, R. W., Selby, J. E. A., Volz, F. E., and Garing, J. S., 1972, Optical properties of the atmosphere (3d ed.): Air Force Cambridge Research Laboratories, Bedford, Mass., 108 p., NTIS AD-753 075.

Monteith, J. L., 1973, Principles of environmental physics: London, Arnold, 241 p.

Myrup, L. O., 1969, A numerical model of the urban heat island: Journal of Applied Meteorology, v. 8, no. 6, p. 908–918.

NASA/Skylab, 1973, Earth resources production processing requirements for electronic sensors Rev. A, Ch. 2, Sec. 5 (PHO-TR524): Johnson Spacecraft Center, Houston, 34 p.

Nicholas, F. W., 1974, Parameterization of the urban fabric: a study of surface roughness with application to Baltimore, Maryland: Unpublished Ph.D. dissertation available on microfilm at the University of Maryland, College Park.

Outcalt, S. I., 1971, A numerical surface climate simulator: Geographical Analysis, v. 3, p. 379–393.

——— 1972a, A reconnaissance experiment in mapping and modeling the effect of land use on urban thermal regimes: Journal of Applied Meteorology, v. 11, no. 8, p. 1369–1373.

——— 1972b, The development and application of a simple digital surface climate simulator: Journal of Applied Meteorology, v. 11, no. 4, p. 629–636.

——— 1972c, A synthetic analysis of seasonal influences in the effects of land use on the urban thermal regime: Archiv fur Meteorologie, Geophysik, und Bioklimatologie, ser. B, v. 20, p. 253–260.

Pease, R. W., 1971, Mapping terrestrial radiation emission with a scanning radiometer: 7th International Symposium on Remote Sensing of the Environment, Ann Arbor, Michigan, 1971, Proceedings, v. 1, p. 501–510.

Pease, R. W., and Nichols, D. A., 1976, Energy balance maps from remotely sensed imagery: Photogrammetric Engineering and Remote Sensing, v. 42, no. 11, p. 1367–1374.

Pease, S. R., and Pease, R. W., 1972, Photographic films as remote sensors for measuring albedos of terrestrial surfaces: U.S. Geological Survey Interagency Report USGS-225, 43 p.

Rayner, J. N., 1971, An introduction to spectral analysis: London, Pion Ltd., 174 p.

Reifsnyder, W. E., and Lull, H. W., 1965, Radiant energy in relation forests: U.S. Department of Agriculture, Forest Service Technical Bulletin 1344, 111 p.

Scott, W. E., Stephens, E. R., Hanst, P. L., and Doerr, R. C., 1957, Further developments in the chemistry of the atmosphere: Proceedings of the American Petroleum Institute, v. 37, p. 171–183.

Sellers, W. D., 1965, Physical climatology: Chicago, University of Chicago Press, 272 p.

Terzaghi, Karl, 1952, Permafrost: Journal of Boston Society of Civil Engineering, v. 39, p. 319–368.

U.S. Geological Survey, 1973, Central Atlantic Region Ecological Test Site (CARETS) map, Baltimore sheet, 1:100,000: U.S. Geological Survey open file report 74–148.

Watson, Ken, Rowan, L. C., and Offield, T. W., 1971, Application of thermal modeling in the geologic interpretation of IR images: International Symposium on Remote Sensing of the Environment, 7th Ann Arbor, Michigan, 1971, Proceedings, v. III, p. 2017–2042.

Wolfe, W. L., ed., 1965, Handbook of military infrared technology: Office of Naval Research, Washington, D.C., 906 p.

☆ U.S. GOVERNMENT PRINTING OFFICE: 1980 O— 311-344/187